Int. J. Solids Structures Vol. 30, No. 11, pp. 1429–1459, 1993
Printed in Great Britain

0020-7683/93 $6.00+.00

MICROMECHANICAL ANALYSIS OF MULTIPLE FRACTURE AND EVALUATION OF DEBONDING BEHAVIOR FOR FIBER-REINFORCED COMPOSITES

SHUH-HUEI LI, SURENDRA P. SHAH, ZONGJIN LI and TOSHIO MURA
National Science Foundation Center for Science and Technology of Advanced Cement-Based Materials, Northwestern University, Evanston, IL 60208, U.S.A.

(*Received* 12 *July* 1992; *in revised form* 16 *October* 1992)

Abstract—Enhanced stress capacity during multiple matrix cracking in unidirectional, continuous fiber-reinforced brittle matrix composites subjected to uniaxial tension has been investigated by using the energy approach of fracture mechanics, in which the bridging stress of the fibers in the matrix crack is determined by the inclusion method. The interactions among the multiple fracture, the interfacial debonding and the frictional sliding are discussed. Theoretical predictions for the stresses at the end point of multiple cracking and the debonding lengths have been derived. To verify the validity of the theoretical model, an experimental study was conducted with cement-based composites made with different volume fractions of steel fibers. The steel fiber reinforced specimens were loaded under uniaxial tension to various pre-determined stress (deformation) magnitudes, and then the deformations in the specimen were "frozen" by gluing rigid steel blocks on the specimen. The technique of optical fluorescence microscopy was used to acquire the extent of debonding length quantitatively from thin sectioned samples obtained by cutting the "frozen" specimen. A "stable growth" of debonding was observed in the study. The theoretical predictions are compared with the experimental results and a reasonable agreement is shown.

1. INTRODUCTION

The mechanical properties of monolithic-brittle materials can be improved by high strength ductile fibers. Enhanced stress capacity and multiple matrix cracking have been observed from the stress–strain curve of the uniaxial tensile test for steel, glass and synthetic fiber-reinforced cementitious composites (Shah, 1991). The toughness enhancement of the matrix involves considerations of cracking of matrix, interfacial debonding, frictional shear resistance along the fiber-matrix region and fiber bridging effect in the cracks. Typically, there are two specified points (points B and C in Fig. 1) in the stress–strain curve to distinguish three stages of mechanical behavior. The first matrix crack is initiated between points A and B, and propagates completely leaving the bridging fiber intact (if the fiber is strong enough) when the path reaches the point B, namely the Bend-Over Point (BOP). Any incremental loading of fibers is transferred back into the matrix which can lead to the second matrix crack at a distance behind the surface of the first crack. Similar to the first crack, the second crack propagates completely when the loading increases up to a certain value. Next, the third crack initiates and propagates and so on. This multiple cracking stage is accompanied by debonding followed by frictional sliding along fiber–matrix interfaces on both sides of the surface of matrix crack. Point C marks the end of multiple matrix cracking. After the point C no further cracking is expected, and the additional load is only sustained by fibers.

A number of studies about the fracture mechanism of the fiber-reinforced, brittle matrix composites have addressed this phenomena. Assuming that the multiple matrix cracking occurred under a constant external load, Aveston *et al.* (1971) used an energy balance method to predict it for the unbonded fiber–matrix interface. Later, Aveston and Kelly (1973) further considered the bonded case. Marshall *et al.* (1985) evaluated crack growth for two different situations (long crack limit and short crack limit) by using either energy balance or balance of stress intensity factor. In the present paper, a theoretical model based on a micromechanical method (the inclusion method) has been proposed to examine the behavior of multiple cracking and the enhanced stress capacity of the matrix. The transverse cracking mode inside a half-space (elastic, matrix) body with periodic loads is introduced to simulate fracture behaviors prior to and posterior to the BOP. The process

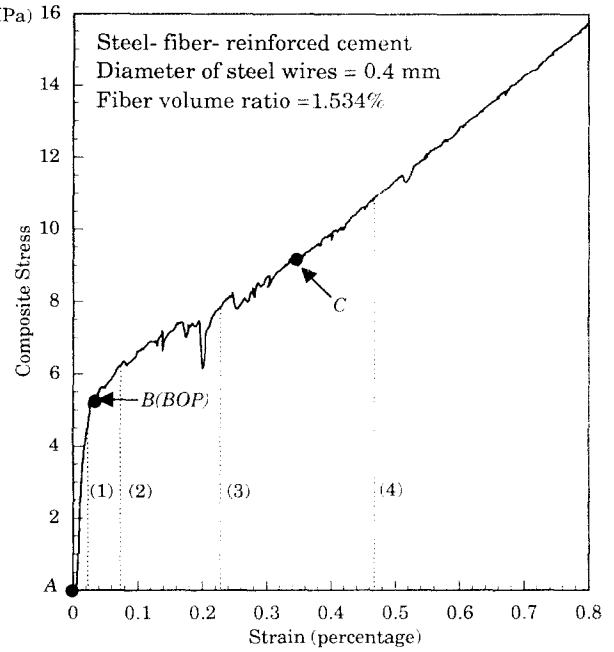

Fig. 1. A typically tensile stress/strain response of steel fiber-reinforced, cementitious composites with fiber volume fraction $f = 1.534\%$ and fiber radius $r = 0.2$ mm, and the four discrete stress levels: (1) $\sigma_A = 4.8$ MPa (before the BOP); (2) $\sigma_A = 6.4$ MPa (between the BOP and point C); (3) $\sigma_A = 7.9$ MPa; and (4) $\sigma_A = 11.$ MPa (beyond point C) are shown.

of the crack growth is considered as follows: (i) initiation and growth of a matrix crack, (ii) initiation of interfacial debonding and sliding, and (iii) formation of complete matrix cracking. This sequence repeats during subsequent, multiple cracking. The applied stress at the end point of the multiple cracking (point C) is then determined.

Studies have been reported which either analyse the interfacial debonding theoretically (Marshall and Oliver, 1987; Wells and Beaumont, 1985; Gao *et al.*, 1988; Hutchinson and Jensen, 1990; Nair, 1990) or inspect the debonding zones experimentally (Campbell *et al.*, 1990). Marshall and Oliver (1987) used the experimental measurement (fiber push-out test) to analyse interfacial debonding and frictional sliding. Hutchinson and Jensen (1990) used approximate closed-form solutions to model the debonding and pullout with two idealizations of friction: constant friction and Coulomb friction. Campbell *et al.* (1990) used transmission electron microscopy to observe the interfacial failure for the SiC-whisker toughened Al_2O_3 and Si_3N_4 materials. The role of the interface in ceramic matrix composites has been recently studied by Evans *et al.* (1991). Fracture surfaces were examined in a scanning electron microscope, and numerical and analytical crack growth simulations were compared with experimental results by Zok *et al.* (1991). In the present study, uniaxial tensile tests were conducted with steel fiber-reinforced cementitious system. After that, the debonding phenomena were examined using the technique of optical fluorescence microscopy (OFM). Finally, experimental results are compared with the present theory and other published prediction.

2. THEORETICAL BACKGROUND

Multiple fracture has been considered previously by some workers (Aveston *et al.*, 1971; Aveston and Kelly, 1973; Marshall *et al.*, 1985). They assumed that the first matrix crack is of prime concern, and did not consider an increase in stresses during multiple fracture. However, a significant increase in external stresses has been observed during the stage of multiple cracking (Somayaji and Shah, 1981; Mobasher *et al.*, 1990). In addition, the influence of energy consumed due to debonding and frictional sliding on the growth of matrix cracking is often not included in theoretical analysis. The model proposed here

considers the enhanced stresses during the multiple cracking stage (point B to C in Fig. 1) as well as the enhanced toughness due to the fiber–matrix debonding and sliding.

2.1. *Mathematical model*

A stage of the composite after BOP is depicted in Fig. 2. A second crack of length $2a$ has formed at a distance of $l_c + l_d^{(0)}$ from the first complete matrix crack. Note that the length l_c is determined by subtracting the extent of debonding $l_d^{(0)}$ of the first crack from the crack spacing. It is assumed that a constant frictional stress τ_f is acting over the debonding length $l_d^{(0)}$. The solution of the problem is simplified by shifting the origin from the crack surface to the place just above the debonded crack tip (Budiansky *et al.*, 1986). It is assumed that a second crack is in a semi-infinite domain defined by $x_3 \geqslant 0$, subjected to a uniform tensile stress σ_A on the far field (x_3 goes to ∞), and a periodic stress over the surface $x_3 = 0$ (as shown in Fig. 3). The shape of the second crack is modeled by a thin spheroid as

$$\Omega_0 : \frac{x_1^2 + x_2^2}{a^2} + \frac{(x_3 - l_c)^2}{c^2} \leqslant 1, \quad \frac{c}{a} \ll 1, \tag{1}$$

where a corresponds to the radius of the crack. $2c$ is the maximum width of the crack, and length, l_c is the distance from position $x_3 = 0$ to the crack center. If the number of fibers intersected by the matrix crack Ω_0 is N, the total bridged domain Ω for the fiber in the matrix crack is equal to $\sum_{i=1}^{N} \Omega_i$. The cross-section of a typical ith fiber with a radius of r is

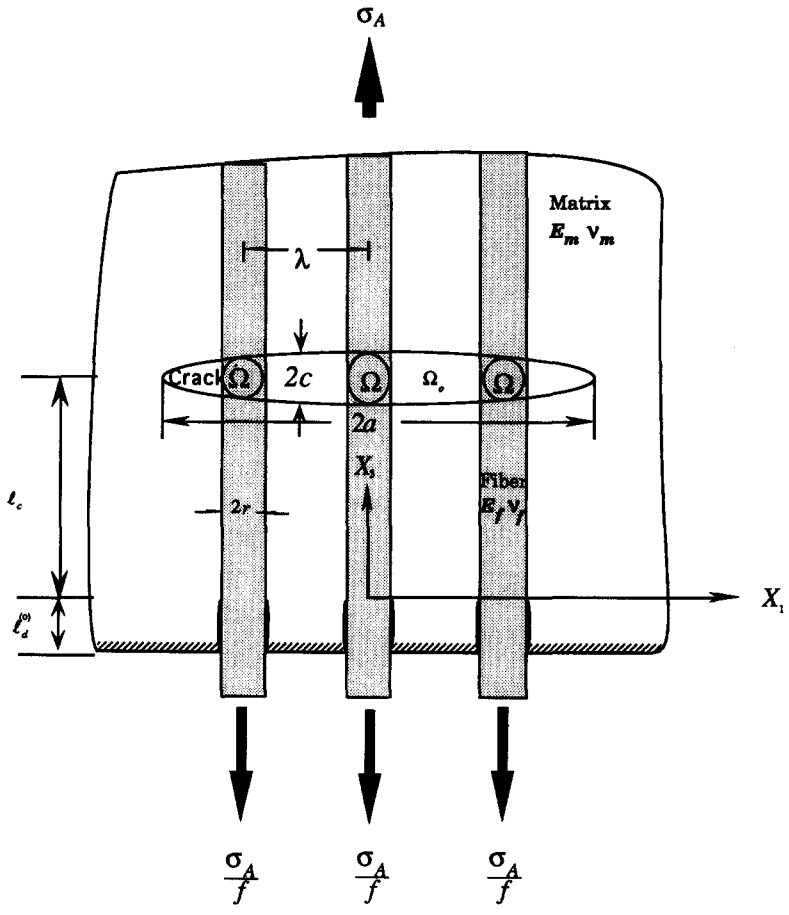

Fig. 2. A schematic drawing shows that typical crack and bridged domains are simulated by ellipsoidal inclusions Ω_0 and Ω subjected to the boundary conditions in a semi-infinite, fiber-reinforced composite, respectively.

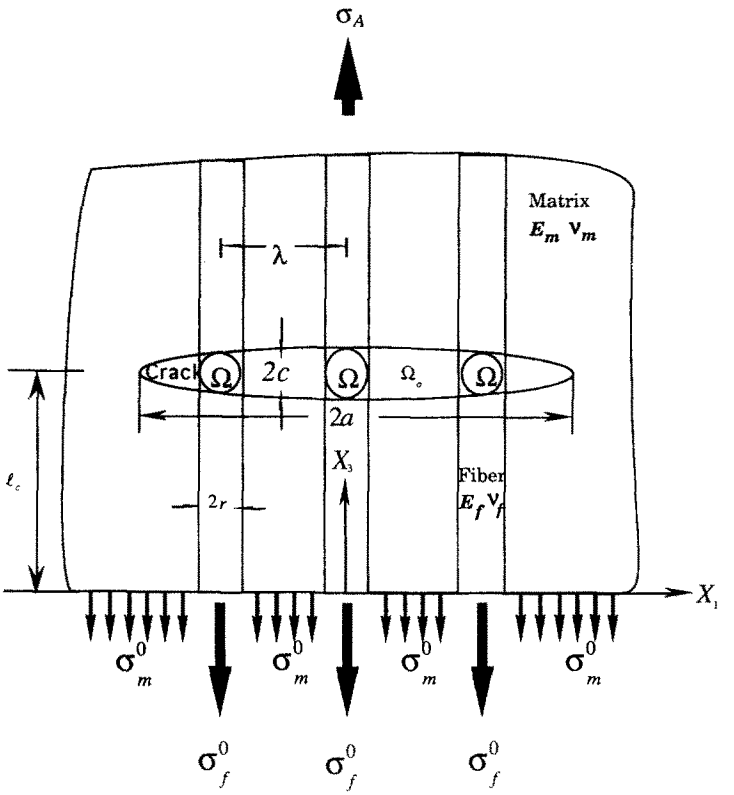

Fig. 3. For the purpose of mechanical analysis, resetting the boundary condition of Fig. 2 to be a periodic stress over the surface $x_3 = 0$ in a semi-infinite, fiber-reinforced composite is shown.

approximated as

$$\Omega_i : \frac{x_1^2 + x_2^2}{r^2} + \frac{(x_3 - l_c)^2}{c^2} \leqslant 1, \quad \frac{c}{r} \ll 1. \tag{2}$$

The fibers are aligned parallel to the x_3-axis with an average spacing λ.

Relations between the average bridging stress of fibers in the crack, length l_c and applied stress can be derived by dividing the system into two parts (Fig. 4). The first part is treated as a half-space elastic body subjected to the boundary conditions (external stresses) without a matrix crack in the composite. In the second part, fictitious misfit strains (eigenstrains) are introduced to simulate the regions of a crack and the bridging parts. Therefore, the stress disturbance due to the crack in the composite can be calculated. Finally, average bridging stress is determined by superposition of both parts.

2.2. *Stress field in elastic part (the uncracked composite)*

The isolated-cylindrical element (Fig. 5) (Wells and Beaumont, 1985; Gao *et al.*, 1988; Hutchinson and Jensen, 1990) can be used to characterize the axial stresses of a fiber and matrix for an uncracked body in any section perpendicular to the x_3-axis, if the interaction among fibers is negligible. Because of the relaxation effect in previous debonding regions, the interfacial shear stress τ_r (bonded interfaces) above the debonding tip won't exceed the shear strength (Sutcu and Hillig, 1990). Consequently, no further debond can be expected. Based on the shear lag model, solving the stresses of the fiber σ_f^A and matrix σ_m^A in the cylindrical composite is similar to the procedure in references Hsueh (1988) and Budiansky *et al.* (1986). They are given in Appendix A. From these stresses and using the criteria that the succeeding matrix crack initiates when $\sigma_m^A = \sigma_{mu}$, the tensile strength of the matrix, one can calculate the length l_c and it is given by

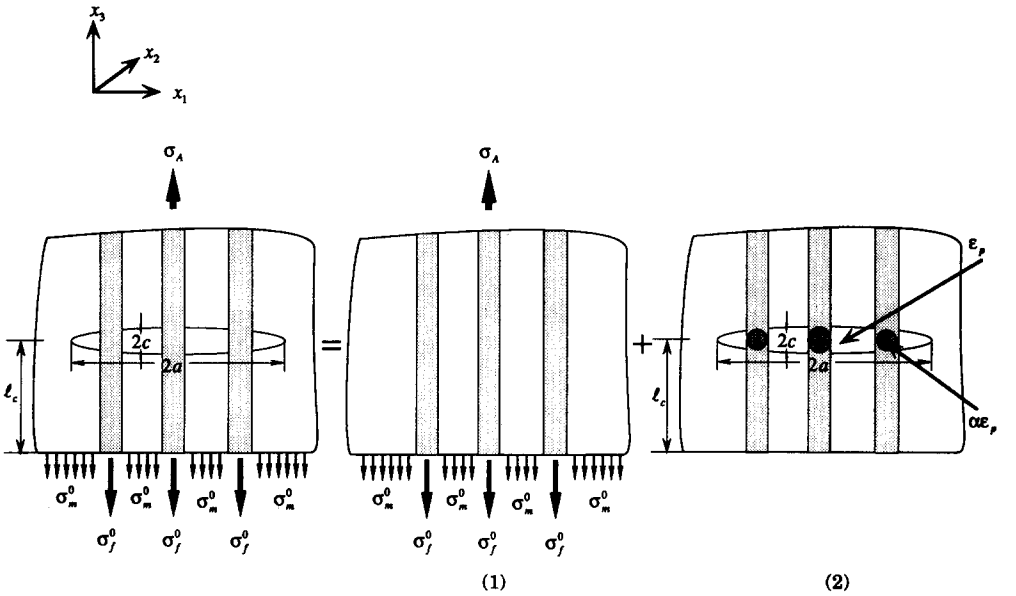

Fig. 4. The stress field in a semi-infinite composite with a matrix crack is obtained by superposition of (1) the part of the uncracked body and (2) the part of the crack disturbance.

$$\frac{l_c}{r} = \frac{-1}{\sqrt{\eta}} \ln\left[-\frac{(A\sigma_A/f + B\sigma_f^\infty - \sigma_{mu})}{B(\sigma_f^0 - \sigma_f^\infty)} \right], \tag{3}$$

where $\sigma_f^\infty = (E_f/\bar{E})\sigma_A$. η, σ_f^0, A and B are defined in Appendix A.

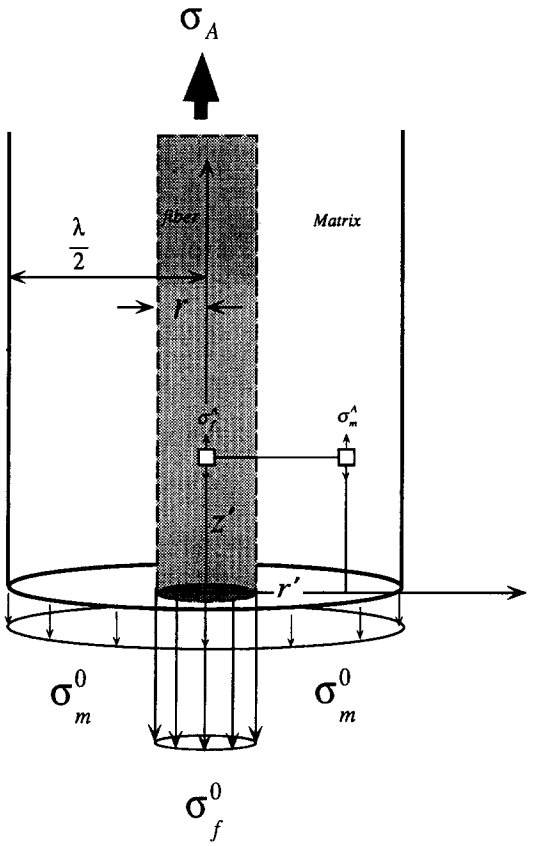

Fig. 5. A schematic drawing shows the coordinate system of an isolated-uncracked element subjected to external stresses.

2.3. *Stress disturbance due to the presence of a crack*

To simulate the disturbance of the stresses caused by a crack, eigenstrains ε_{33}^{*} are introduced into $\Omega_0-\Omega$ (unbridged part of the crack) and Ω (bridged domain) as

$$\varepsilon_{33}^{*}=\begin{cases}\varepsilon_p \in \Omega_0-\Omega's,\\ \alpha\varepsilon_p \in \Omega's,\end{cases} \tag{4}$$

where α is the factor which characterizes the crack opening in the bridged domain Ω. The factor α also characterizes the fiber sliding along the interfaces: $\alpha=1$ is a plain matrix; $\alpha=0$ implies a matrix with complete fibers bridging, i.e. perfect bond between fibers and the matrix; and $0<\alpha<1$ if debonding and sliding take place in the interface. The value of α is the function of aspect ratio (crack length/fiber radius), interfacial friction stress and other material constants. To solve a problem concerning a crack domain Ω_0 in a semi-infinite body with fiber bridged part Ω, first the stress field for the point interior to Ω_0 when the eigenstrain ε_p is introduced in Ω_0 is determined. Next, the stress field in Ω_0 when eigenstrain $-(1-\alpha)\varepsilon_p$ is employed only in the bridged part Ω is ascertained. The final stress field for the points interior to the crack Ω_0 can then be obtained from the sum of both parts (see Fig. 6).

The details of the formulation are given in Appendix B. This linear superposition leads to the bridging stress of the fiber σ_T as

$$\sigma_T=\frac{(1-\alpha)a/r}{1+\beta(a/l_c)+(1-\alpha)f(a/r)}\xi\sigma_A, \tag{5}$$

and the value of the bridging factor α as

$$\alpha=\frac{1}{2(a/r)(f+\kappa)}\left\{1+\frac{a}{r}\left[2\kappa+f+\beta\left(\frac{r}{l_c}\right)\right]-\left\{\left\{1+\frac{a}{r}\left[2\kappa+f+\beta\left(\frac{r}{l_c}\right)\right]\right\}^2-4\kappa(f+\kappa)\left(\frac{a}{r}\right)^2\right\}^{1/2}\right\}, \tag{6}$$

where

$$\xi=\left[1+\frac{(1-f)}{f}\frac{E_m}{E_f}\exp\left(-\sqrt{\eta}\frac{l_c}{r}\right)\right], \tag{7}$$

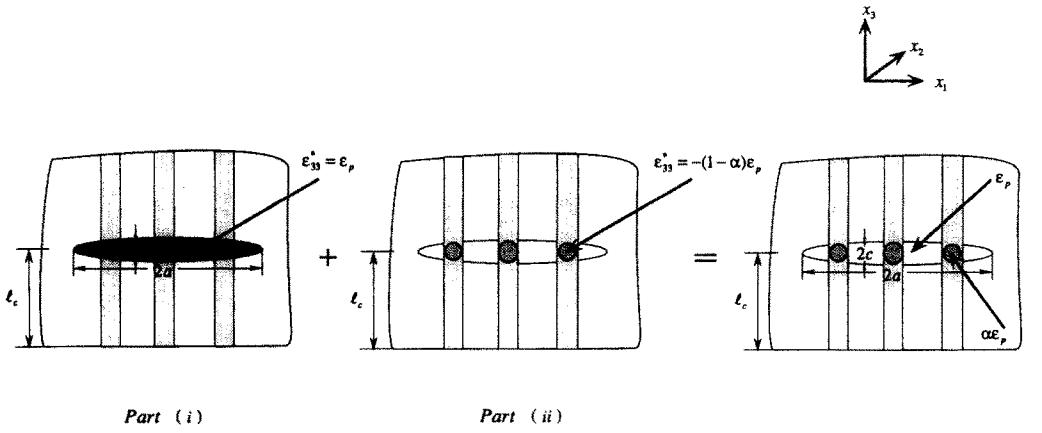

Fig. 6. The disturbed stress field in the semi-infinite composite with a matrix crack can be calculated by introducing two eigenstrains: (i) the eigenstrain ε_p in domain Ω_0 and (ii) $-(1-\alpha)\varepsilon_p$ in the unbridged domain Ω.

and

$$\kappa = \frac{\pi\bar{\mu}(1-f)E_m}{8\tau_f(1-\bar{\nu})E_f\bar{E}}\xi\sigma_A. \tag{8}$$

3. DETERMINATION OF DEBONDING LENGTH IN A CRACK

The debonding length is determined from energy considerations (Wells and Beaumont, 1985) and using concepts of fracture mechanics. It is assumed that when a debonding crack propagates, the length of the matrix crack ($2a$) remains unchanged. It is also assumed that all fibers associated with the debonding inside the matrix crack have identical debonding length.

In order to use the energy approach, the debonding and frictional sliding along the fiber–matrix interface can be treated as extensions of a debonding crack. A typical cylindrical element (Gao *et al.*, 1988) has been chosen to calculate the energy change when the debonding crack grows (Fig. 7). If the stresses above the debonding front remain unchanged (Budiansky *et al.*, 1986), then energy changes in this isolated cell when the debonding crack grows by an incremental amount $2\pi r\,\mathrm{d}(l_d)$ come from: (i) potential energy release $\mathrm{d}W_P$, which includes the increment in the elastic strain energy of fiber/matrix $\mathrm{d}W_E$ and work done by external load (bridging stress) $\mathrm{d}W_L$; and (ii) frictional work $\mathrm{d}W_F$ along the debonding zone. The surface energy for debonding crack must be balanced by the increment of released energy deducting the amount of frictional energy dissipation for the system (cylindrical cell), that is

$$\begin{aligned}\mathrm{d}W_{\gamma^*} &= -\mathrm{d}W_P - \mathrm{d}W_F \\ &= \mathrm{d}W_L - \mathrm{d}W_E - \mathrm{d}W_F,\end{aligned} \tag{9}$$

where

$$\mathrm{d}W_L = \frac{r\tau_f^2}{2E_f}\left[-\frac{\sigma_T^2}{\tau_f^2} + \frac{2}{(1-f)}\frac{\bar{E}}{E_m}\frac{\sigma_T}{\tau_f}\left(\frac{l_d}{r}\right)\right]\cdot 2\pi r\,\mathrm{d}(l_d), \tag{10}$$

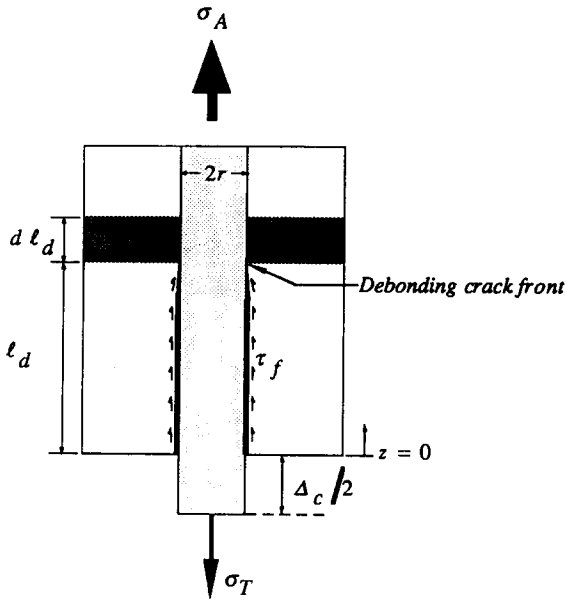

Fig. 7. An isolated element with debonding crack l_d is shown. The energy change in this element can be calculated if debonding crack increases $\mathrm{d}(l_d)$.

$$dW_E = \frac{r\tau_f^2}{4E_f}\left[\frac{\sigma_T^2}{\tau_f^2} + \frac{4}{(1-f)}\frac{\bar{E}}{E_m}\left(\frac{l_d}{r}\right)^2 - 4\frac{\sigma_T}{\tau_f}\left(\frac{l_d}{r}\right)\right]\cdot 2\pi r\, d(l_d), \tag{11}$$

$$dW_F = \frac{r\tau_f^2}{E_f}\left[-\frac{2}{(1-f)}\frac{\bar{E}}{E_m}\left(\frac{l_d}{r}\right)^2 + \frac{\sigma_T}{\tau_f}\left(\frac{l_d}{r}\right)\right]\cdot 2\pi r\, d(l_d), \tag{12}$$

$$dW_{\gamma^*} = 2\gamma^*\cdot 2\pi r\, d(l_d). \tag{13}$$

All terms in eqns (10)–(13) are derived in Appendix C. Using the Griffith type of energy balance, which is

$$\frac{\partial W_{\gamma^*}}{\partial(2\pi r l_d)} = 2\gamma^* = -\frac{\partial W_P}{\partial(2\pi r l_d)} - \frac{\partial W_F}{\partial(2\pi r l_d)}, \tag{14}$$

leads to a value of l_d as follows:

$$\frac{l_d}{r} = \frac{\sigma_T}{2\tau_f}\left\{1 - \left[\frac{fE_f}{\bar{E}} + \frac{(1-f)E_m}{\bar{E}}\left(\frac{\sigma_T^i}{\sigma_T}\right)^2\right]^{1/2}\right\}, \tag{15}$$

where γ^* is debonding surface energy, σ_T is given from eqn (5) and

$$\sigma_T^i = \left(\frac{8E_f\gamma^*}{r}\right)^{1/2}. \tag{16}$$

Generally, the debonding process may be either a stable or an unstable growth. However, if we consider the derivative of eqn (14), it can be pointed out that the analysis of the present model for the debonding crack is a steady-state consideration. This is consistent with experimental observation (see Section 6). The extent of the debonding tends to be small if frictional shear stress τ_f is large. In addition, the extent of debonding is also reduced when the interfacial toughness γ^* increases.

4. FRACTURE PROCESS OF A MATRIX CRACK IN THE SEMI-INFINITE COMPOSITES

A typical matrix crack propagation in the multiple cracking range involves three critical points: (i) complete bridging; (ii) initiation of debonding/sliding; and (iii) complete matrix cracking. Each point characterizes different fracture behavior, e.g. extension of matrix crack, interfacial debonding/sliding at a constant matrix crack length and complete crack growth. These three cases are examined below.

Based on the energy criterion (fracture mechanics), the total potential energy W (i.e. the mechanical Gibbs free energy), defined by the sum of the elastic strain energy and potential energy of external loads, is first calculated as follows:

$$\begin{aligned} W &= \frac{1}{2}\int_D \sigma_{ij}^T \varepsilon_{ij}^e\, dD - \int_S \sigma_{ij}^A n_j u_i\, dS \\ &= \frac{-1}{2}\int_{\Omega_0} \sigma_{33}\varepsilon_{33}^*\, dV - \int_{\Omega_0} \sigma_{33}^A \varepsilon_{33}^*\, dV \\ &= W_0 \frac{1+\beta\dfrac{a}{l_c} + (1-\alpha^2) f\dfrac{a}{r}}{\left[1+\beta\dfrac{a}{l_c} + (1-\alpha) f\dfrac{a}{r}\right]^2}, \end{aligned} \tag{17}$$

where

$$\sigma_{ij}^{T} = \sigma_{ij} + \sigma_{ij}^{A}, \quad \varepsilon_{ij}^{e} = \varepsilon_{ij} - \varepsilon_{ij}^{*},$$
$$\sigma_{33}^{A} = \xi\sigma_{A},$$
$$W_0 = \frac{-4(1-\bar{\nu})a^3}{3\bar{\mu}}\xi^2\sigma_A^2. \tag{18}$$

Note that σ_{33} is defined by eqns (B16) and (B17), and ε_{33}^{*} is defined by eqn (4).

4.1. *The state of complete bridging*

For the case of complete bridging, the matrix crack is reinforced by fibers but no debonding along interfaces takes place, and bridging factor α is equal to zero. The Gibbs free energy and energy release rate for the extension of the matrix crack, defined by $G = -\partial W/\partial(\pi a^2)$, can be determined as:

$$W = W_0 \frac{1}{1+\beta\left(\frac{a}{l_c}\right)+f\frac{a}{r}}, \tag{19}$$

and

$$G = G_0 \frac{1+\frac{2}{3}\left[\beta\left(\frac{a}{l_c}\right)+\left(\frac{a}{r}\right)f\right]}{\left[1+\beta\left(\frac{a}{l_c}\right)+f\left(\frac{a}{r}\right)\right]^2}, \tag{20}$$

where

$$G_0 = \frac{2(1-\bar{\nu})a}{\pi\bar{\mu}}\xi^2\sigma_A^2. \tag{21}$$

The matrix crack does not grow until the energy release rate G reaches the fracture toughness of matrix G_c $(=2\gamma)$, i.e. $G = G_c$, where γ is the matrix surface energy.Therefore, the critical value of the external stress just before the crack extends is given by

$$\sigma_A = \left[\frac{\pi\bar{\mu}\gamma}{(1-\bar{\nu})a\xi^2}\right]^{1/2}\left(1+\frac{a}{r}f+\beta\frac{a}{l_c}\right)\left(1+\frac{2}{3}\frac{a}{r}f+\frac{2}{3}\beta\frac{a}{l_c}\right)^{-1/2}. \tag{22}$$

Equation (22) is shown by the group of curves labeled (1) in Fig. 8. The applied stress is plotted as a function of crack size a in Fig. 8 by using the mechanical properties reported in Table 1(a) with the Poisson's ratios $v_f = 0.3$ and $v_m = 0.2$.

Table 1. Material property values of the steel-fiber, cementitious composite systems

	(a)†	(b)
Mix design (by weight)	(Cement : Water) 1 : 0.35	(Cement : Sand : Water) 1 : 2 : 0.5
Curing time (days)	14	28
Matrix modulus (GPa)	14	20
Fiber modulus (GPa)	210	190
Frictional shear stress (MPa)	1.3	1.86
Surface energy of matrix (N mm^{-1})	0.0075	0.011
Surface energy of interface (N mm^{-1})	0.0055	0.008

†3.86 ml superplasticizer per kilogram cement was used.

4.2. *The state of initiation of debonding*

As we realize from the previous section, upon the stress reaching the value given by eqn (22), the matrix crack suddenly grows up to a certain size. Consequently, not only the bridging action from fibers prevents the instability of the crack, but the fracture process of matrix cracking now includes interfacial debonding/sliding as well. The situation of initiation of debonding is a transient point to distinguish the fracture behaviors. In order to define the critical condition, the result in eqn (15) (Section 3) could be used to determine the threshold value of external stress for initiation of debonding/sliding with $l_d = 0$, and it is given by

$$\sigma_A = \frac{1}{\xi}\left(\frac{8E_f\gamma^* r}{a^2}\right)^{1/2}\left(1+\beta\frac{a}{l_c}+f\frac{a}{r}\right). \tag{23}$$

Equation (23) is shown by the curve-group (2) in Fig. 8. It is pointed out that threshold stress σ_A [eqn (23)] not only depends on crack size a, but also varies with the length l_c [the position of the matrix crack defined in Fig. 8 as $\Lambda = \beta(r/l_c)$]. For the very first crack in the composite, i.e. $r/l_c \to 0$, with large crack size, the threshold stress calculated from eqn (23) is identical to the results of Gurney and Hunt (1967) and Outwater and Murphy (1969).

4.3. *The state of complete matrix cracking*

After the applied stress reaches the value of eqn (23), the interfacial debonding and frictional sliding accompany the system. The energy dissipations contributed from both effects increase the resistance to keep the crack stable. These total dissipated energies due to sliding W_S and debonding W_D (for $0 < \alpha < 1$) along the slip distances (sliding interfaces) in a crack have been calculated previously by Li *et al.* (1992). They are given by

$$W_S = 2\frac{\pi a^2}{\pi(\lambda/2)^2}\frac{\pi(1-f)^2E_m^2}{12\tau_f E_f \bar{E}^2}\frac{a^3(1-\alpha)^3}{\left[1+\beta\frac{a}{l_c}+(1-\alpha)\frac{a}{r}f\right]^3}\xi^3\sigma_A^3, \tag{24}$$

and

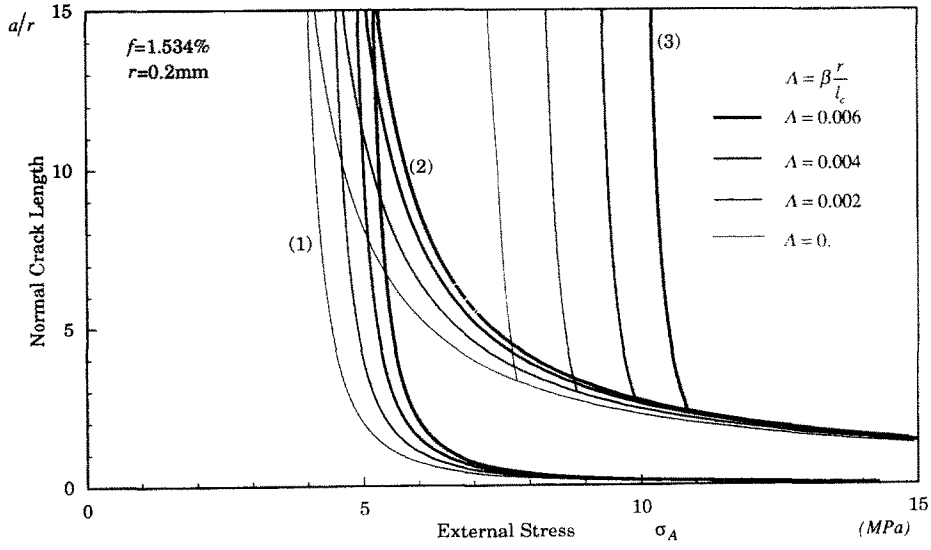

Fig. 8. Relationships between external stress and normalized crack length for the cases of (1) the perfect bond, (2) the initiation of debonding and (3) the complete matrix cracking become tougher and tougher as Λ increases by using material properties reported in Table 1(a) with $\nu_f = 0.3$ and $\nu_m = 0.2$ for $f = 1.534\%$, $r = 0.2$ mm.

$$W_D = 2\frac{\pi a^2}{\pi(\lambda/2)^2}\frac{\pi r(1-f)E_m\gamma^*}{\tau_f \bar{E}}\frac{(1-\alpha)a}{\left[1+\beta\dfrac{a}{l_c}+(1-\alpha)\dfrac{a}{r}f\right]}\xi\sigma_A, \tag{25}$$

where the factor 2 counts as the debonding/sliding along both the upper and lower parts of the fibers, and $\pi a^2/\pi(\lambda/2)^2$ is the number of fibers in the crack. Therefore, the energy change rate for sliding ΔG_S and debonding ΔG_D can be obtained by taking the derivative of eqns (24) and (25) with respect to (πa^2), i.e.

$$\begin{aligned}\Delta G_S &= \frac{\partial(W_S)}{\partial(\pi a^2)}\\ &= \frac{f(1-f)^2(1-\alpha)^2(E_m/\bar{E})^2 a\Gamma}{12E_f\tau_f}\xi^3\sigma_A^3\\ &\quad\times\frac{\{5(1-\alpha)\Gamma+2(1-\alpha)\Gamma^2\Lambda+2(1-\alpha)^2\Gamma^2 f+3[-a\Gamma(\partial\alpha/\partial a)](1+\Gamma\Lambda)\}}{\{1+\Gamma\Lambda+(1-\alpha)\Gamma f\}^4},\end{aligned} \tag{26}$$

and

$$\begin{aligned}\Delta G_D &= \frac{\partial(W_D)}{\partial(\pi a^2)}\\ &= \frac{\gamma^* f(1-f)(E_m/\bar{E})}{\tau_f}\xi\sigma_A\\ &\quad\times\frac{\{3(1-\alpha)\Gamma+2(1-\alpha)\Gamma^2\Lambda+2(1-\alpha)^2\Gamma^2 f+[-a\Gamma(\partial\alpha/\partial a)](1+\Gamma\Lambda)\}}{\{1+\Gamma\Lambda+(1-\alpha)\Gamma f\}^2},\end{aligned} \tag{27}$$

where

$$-\left(\frac{\partial\alpha}{\partial a}\right)a\Gamma = \frac{1}{2(f+\kappa)}\left[1-\frac{(f+\Lambda+2\kappa)\Gamma+1}{\{[1+\Gamma(f+\Lambda+2\kappa)]^2-4\kappa(f+\kappa)\Gamma^2\}^{1/2}}\right], \tag{28}$$

and

$$\Gamma = \frac{a}{r}, \qquad \Lambda = \beta\frac{r}{l_c}. \tag{29, 30}$$

The energy release rate G for the matrix extension is then given by

$$\begin{aligned}G &= -\frac{\partial F}{\partial(\pi a^2)}\\ &= \frac{2(1-\bar{\nu})a\xi^2\sigma_A^2}{3\pi\bar{\mu}\{1+\Gamma\Lambda+(1-\alpha)\Gamma f\}^3}\\ &\quad\times\left\{\left[3+4\Gamma\Lambda+4(1-\alpha^2)f\Gamma+2\alpha f\left[-\left(\frac{\partial\alpha}{\partial a}\right)a\Gamma\right]\right][1+\Lambda\Gamma+(1-\alpha)f\Gamma]\right.\\ &\quad\left.-2[1+\Lambda\Gamma+(1-\alpha^2)f\Gamma]\left[\Gamma\Lambda+(1-\alpha)f\Gamma+f\left[-\left(\frac{\partial\alpha}{\partial a}\right)a\Gamma\right]\right]\right\}.\end{aligned} \tag{31}$$

In order to determine the critical condition of complete matrix cracking, debonding and sliding should be included in the Griffith energy criteria. It follows that

$$G-\Delta G_S-\Delta G_D = G_C. \tag{32}$$

With the use of eqns (26), (27) and (31), the cracking stress σ_A as a function of crack size can be determined [shown by the curve-group (3) in Fig. 8]. It is noted that the applied stress required to advance a matrix crack is dependent on crack size and length l_c. Thus, the position of a matrix crack along the fiber direction in a semi-infinite body can influence the stress capacity of the composite.

To examine the stability of a crack in a semi-infinite body of fiber-reinforced composites as depicted in Fig. 2, two energy criterions are set to determine crack growth: (i) $G = R$ and (ii) $\partial G/\partial(\pi a^2) = \partial R/\partial(\pi a^2)$. The resistance R is equal to $G_C+\Delta G_S+\Delta G_D$, while G stands for the energy release rate and G_C stands for the fracture toughness of the matrix. When $G < R$, the crack remains stable; when $G > R$, the crack propagates but becomes stable if $\partial G/\partial(\pi a^2) < \partial R/\partial(\pi a^2)$; if $G > R$, and $\partial G/\partial(\pi a^2) > \partial R/\partial(\pi a^2)$, the propagation of the crack will become unstable. This is demonstrated in Fig. 9, which represents energy release rate G and resistance R against crack size a. As can be seen from Fig. 9, when G reaches the value of G_C, the crack size begins to grow, and suddenly extends to a_e. There is an increase in the value of resistance R from G_C to $G_C+\Delta G_S+\Delta G_D$ at an extended crack length, say a_e. After passing through this transitional region at $a = a_e$, the energy dissipations due to debonding and sliding delay the crack propagation if external stress is smaller than a certain value determined from curve-group (3). However, when G reaches the scale $G_C+\Delta G_S+\Delta G_D$, the instability of the crack size a_e occurs again.

An overall description of the fracture process of a single crack is shown in Fig. 10, which comprises the results as depicted in Fig. 9. The derivation of curves (1), (2) and (3) were detailed in Sections 4.1, 4.2 and 4.3, respectively. In Fig. 10, when external stress is on the left-hand side of curve (1), the matrix crack keeps its original size; upon the stress reaching the value indicated by eqn (22), this crack suddenly extends to the size a_e. If external stress increases further, the interfaces start to debond and fibers continue to slip. Finally, the matrix crack doesn't grow until the stress is equal to the value obtained by eqn (32).

4.4. *The behavior of multiple matrix cracking*

If we consider an increment of Λ (i.e. decrease of l_c), the curves (1), (2) and (3) (plain lines) of Fig. 8 shift to the right (bold lines). It is pointed out that the toughening of the composite increases as l_c decreases. Thus, the length l_c plays an important role in determining toughness G. The process of multiple matrix cracking can be explained as follows. Consider an infinite matrix containing an initial flaw ($\bar{a}_1$ in Fig. 11). This condition is represented by the curve-group represented by $\Lambda = 0$. When the stress reaches the value σ_{A1}, the first matrix crack propagates completely through the entire cross-section of the specimen (at the BOP).

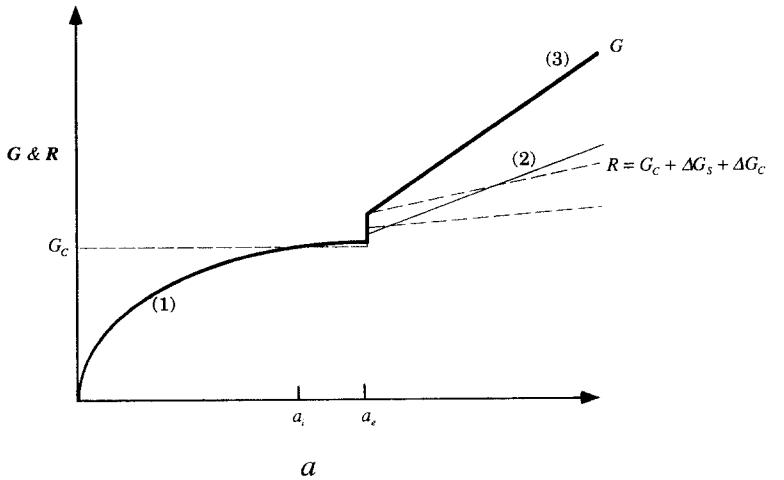

Fig. 9. Energy release rate G and the sum of fracture toughness G_C, frictional resistance ΔG_S, and debonding resistance ΔG_D are plotted versus crack size for the cases of (1) σ_A = eqn (B2), (2) eqn (B2) $< \sigma_A < \sigma_{cr}$ and (3) $\sigma_A = \sigma_{cr}$, where σ_{cr} can be obtained by solving eqn (32).

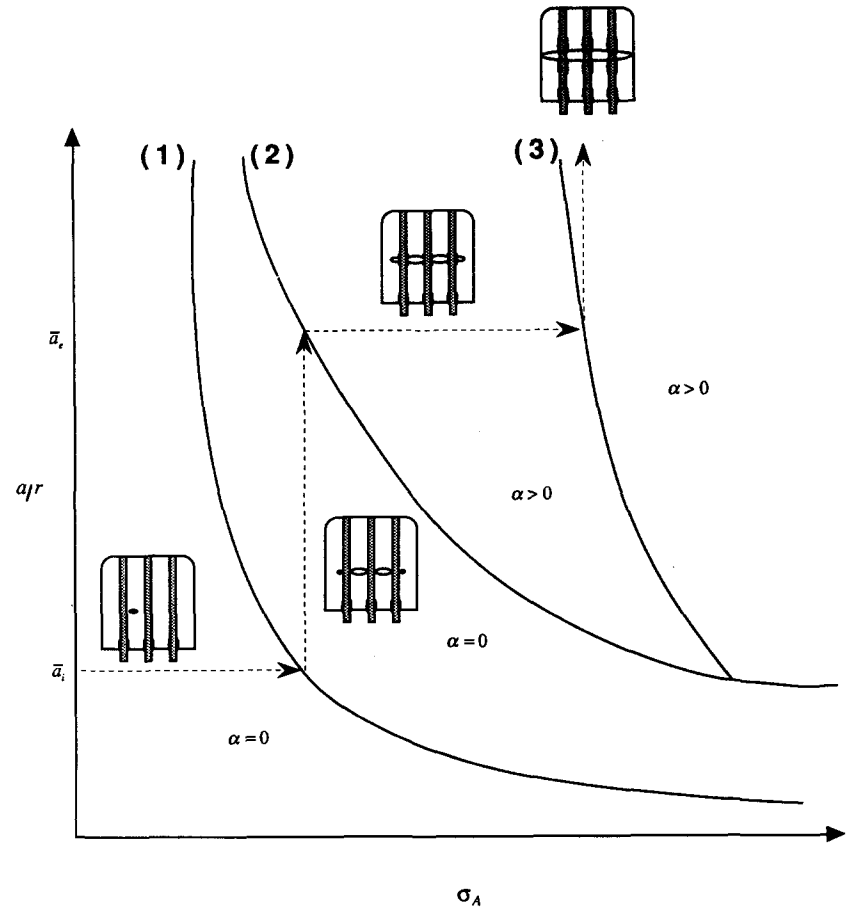

Fig. 10. Normalized crack length versus external stress for the case of (1) the perfect bond, (2) the initiation of debonding and (3) the complete matrix cracking are shown. The path of the crack extension in a semi-infinite, fiber-reinforced composite is indicated by the arrows.

At that time, additional load transferring from fibers to the matrix induces the second crack $l_c + l_d^{(0)}$ away from the surface of the first crack. The geometry of the composite is now changed from infinite space to semi-infinite space with a crack inside the body. As it has been mentioned earlier, curves (1), (2) and (3) in Fig. 8 vary with l_c. The propagation of the second crack proceeds along the arrows (broken lines) as shown in Fig. 11, and extends to infinity if the external stress reaches the value of curve (3) with increasing applied stress from σ_{A1} to σ_{A2}. Similarly, the curves (1), (2) and (3) of succeeding cracks, e.g. matrix crack No. 3 etc., move further to the right of those of the preceding cracks (cracks No. 1 and 2) when the succeeding cracks develop, i.e. as Λ increases. Consequently, it is implied that the behavior of multiple matrix cracks in the composite can strengthen the ability to sustain more stress capacity. Moreover, the process of multiple cracking in the brittle matrix composite, which is related to its stress–strain curve (inset, Fig. 11), can be explained entirely from Fig. 11 (the relationship between σ_A and a).

5. EXPERIMENTAL INVESTIGATION

This experimental part investigated the micromechanisms of matrix fracture by means of quantitative analysis. For this purpose, uniaxial tensile tests of steel fiber reinforced cement-based composites were conducted.

5.1. *Specimen preparation*

Fabrication of the specimens was achieved by using a plexiglass mold. The mold consisted of a base plate, two side plates, two end plates and two guide plates. The guide

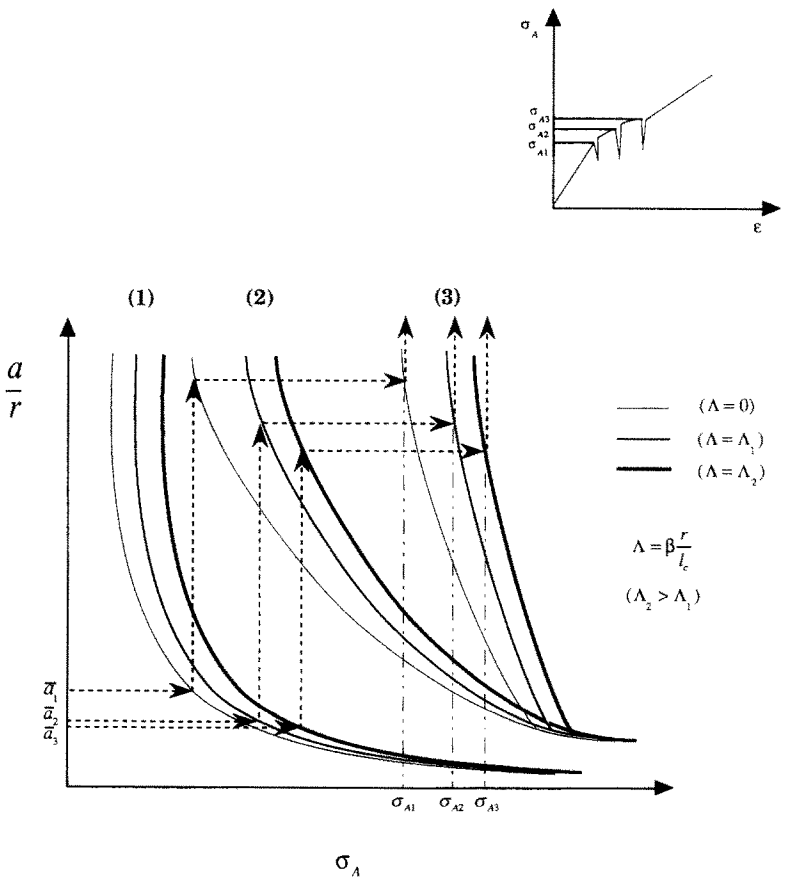

Fig. 11. The schema of relationships between normalized crack length and external stress shows that as Λ increases (i.e. crack spacing decreases), the applied stresses of curves (1), (2) and (3) increase from plain lines to bold lines, respectively. The incremental applied stresses (e.g. from σ_{A1} to σ_{A2}), which corresponds to the stress–strain response, during the multiple cracking stage are shown as well.

plates with 30 holes were used to provide alignment of fibers and to separate the anchorage portion and test portion of specimen during construction. The anchorage part of the specimen was cast with the normal type epoxy resin right after steel fibers were aligned in the mold and fixed outside to the mold frame. Continuous steel wires obtained from Bekaert Co. Chicago, IL, with diameters of 0.2032 mm (0.008 in.), 0.4064 mm (0.00016 in.), and 0.8128 mm (0.0032 in.) were used as fibers. Neat cement paste made of Type I portland cement with a water/cement ratio of 0.35 was used as matrix for tension portion. In order to facilitate the workability, 3.86 ml superplasticizer per kilogram of cement was added into the mixture. The specimens were cast horizontally with the embedded fiber perpendicular to the direction of casting. Three series with different fiber volume fractions, 0.767%, 1.534% and 6.135% were employed in the experimental study. For the specimen series with 0.767% fiber volume fraction, 15 steel wires with a diameter of 0.4 mm were used in each specimen. The number of fibers increased to 30 with the same diameter (0.4 mm) of the fiber for the specimen group of 1.534% volume fraction. Thirty wires with 0.8 mm diameter were used for the specimen series of 6.135%. Specimens were cured in water and tested at 14-day age after the surfaces of the specimen were ground. In general, three groups of tests were identical. No artificial crack was introduced in the specimens.

5.2. *Test set-up and procedure*

The specimen being held in the mechanical fixture is shown in Fig. 12. Two frictional grips were used in the set-up. One of them was connected to the servohydraulic actuator while the other was connected to the load cell. Two Linear Variable Differential Transducers

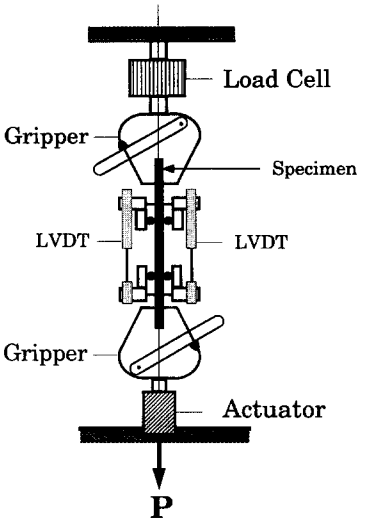

Fig. 12. Experimental set-up for the uniaxial tension test of steel fiber-reinforced cement specimen.

(1.127 mm, or 0.05 in., range), i.e. LVDTs, mounted on the opposite side of the specimen using a 76.4 mm (3 in.) gage length were used to measure the extension of the specimen during loading. The average output of LVDTs was also used as the feedback signal in the control of the servohydraulic system. The uniaxial tensile tests were performed at a rate of 0.000762 mm per minute. Once the specimens were loaded up to the designated displacement level, the mode of the control was switched to force-signal control and a command of holding position was selected at that time. The switching of the control mode was necessary due to the need to remove LVDTs from the set-up. After demounting the LVDTs from the specimen, two rigid steel blocks ($50.8 \times 25.4 \times 12.7$ mm) were glued onto the opposite surfaces of the specimen by using a fast hardening epoxy to "freeze" the opening displacements of matrix cracks at that stress value. When the epoxy adhesive hardened, the specimen was unloaded and removed from the MTS machine. The data of load elongation and stroke were acquired through the TestsStar software in the controlling work station.

5.3. *Study of optical fluorescence microscopy (OFM)*

To quantify the debonding properties of the loaded specimen with the minimal amount of disturbance, the "strain freezed" specimens were treated prior to the study of thin-sectioned samples in an optical microscope. The specimen length was first trimmed off to the section restrained by the steel blocks. Then, the epoxy impregnation procedure (Fig. 13) for the specimen was performed by using low viscosity epoxy (LR white resin from Polysciences, Inc., Warrington, PA) and hardener mixed with fluorescence dye. The dissolution of the dye in epoxy utilized a less viscous medium for transporting the dye into the debonding zone. After impregnation, specimens were then cured at room temperature for 24 hours. The thin sections were prepared by sectioning the specimens longitudinally and grinding using grit size of 320, 400 and 600 with a non-aqueous polishing lubricant. Lapp cloths impregnated with diamond paste of 6 μm, 2 μm, 1μm and 0.25 μm were used in the final polishing of the samples. Figure 14 shows schematically the preparation procedure of thin sections.

The polished thin sections were examined with a fluorescence microscope and an image analysis system to quantify the debonding behavior. It was ensured that the fluorescence dye together with LR white resin would penetrate into the interface if there exist a debonding crack. As an illustration, Fig. 15(a) shows two bright (upper and lower) lines along the boundaries of the fiber and matrix which directly characterize the size of the debonding surface. On the other hand, no dye penetration is observed for the case of bonded interface as shown in Fig. 15(b). Furthermore, in order to observe an entire contact area of the

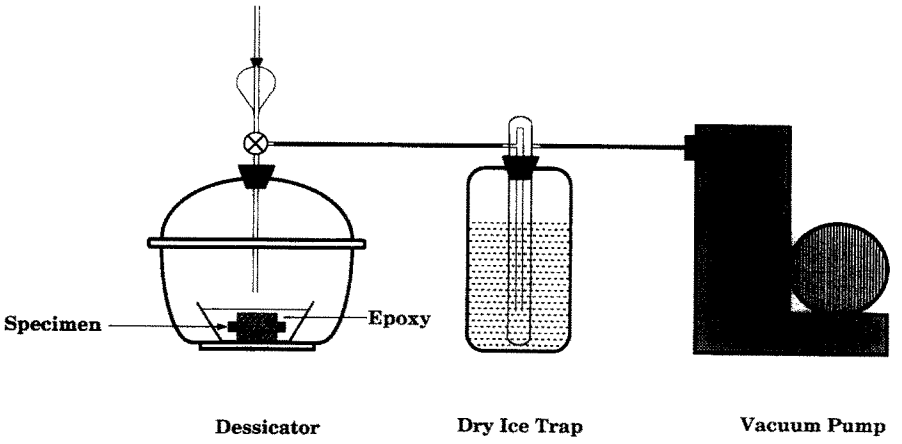

Fig. 13. Schematic drawing of the impregnation procedure.

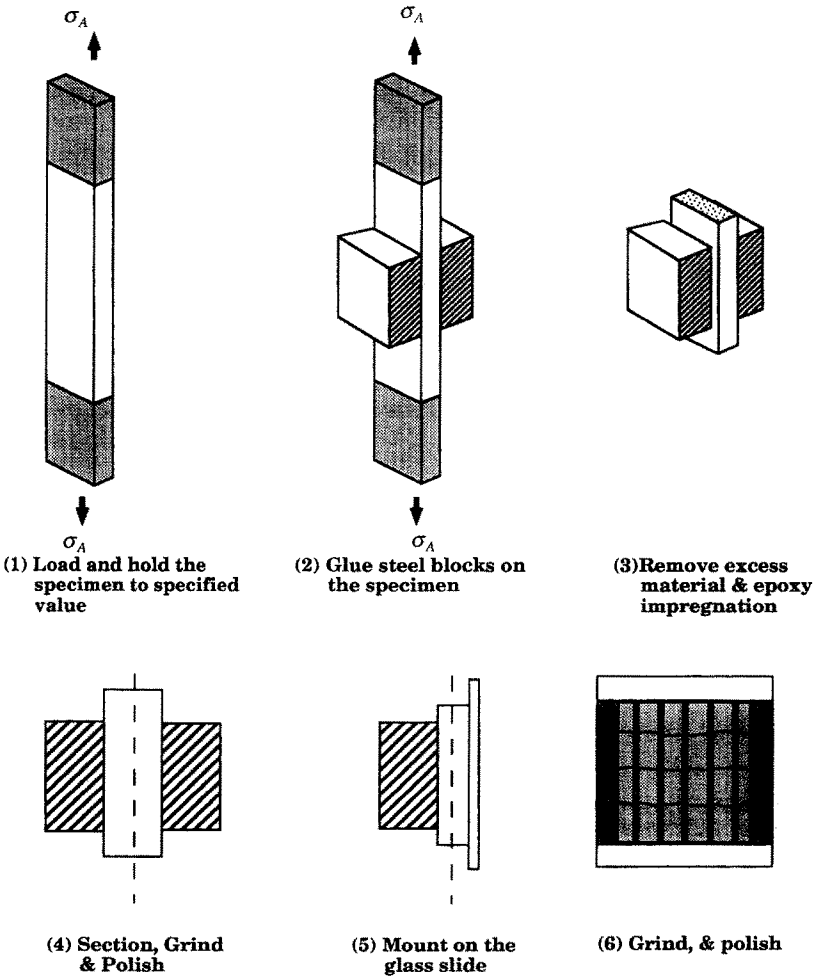

Fig. 14. Preparation of the thin sectioning: (1) load and hold the specimen to specified level, (2) glue steel blocks on the specimen, (3) remove excess material and perform the epoxy impregnation for the specimen, (4) section, grind and polish, (5) mount on the glass slide and (6) grind and polish.

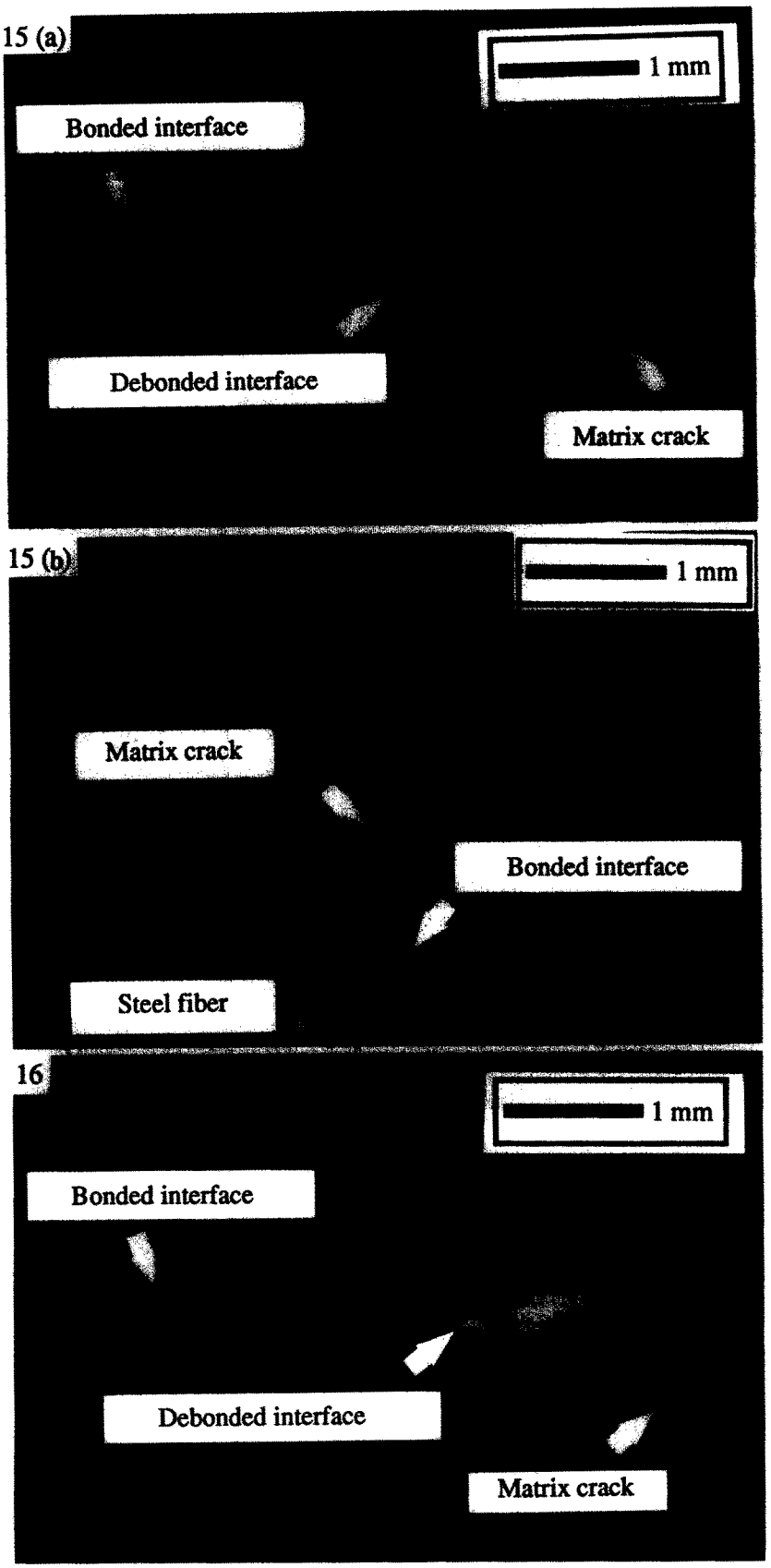

Fig. 15. Illustration of the different view for debonded and bonded interface after impregnation: (a) a typical debonded interface ($f = 1.534\%$ and $\sigma_A = 6.4$ MPa for the first matrix crack) and (b) a typical bonded interface ($f = 6.135\%$ and $\sigma_A = 4.2$ MPa for the first matrix crack).

Fig. 16. View of the entire debonded area after taking out the fiber with $f = 1.534\%$ at $\sigma_A = 6.4$ MPa for the first matrix crack.

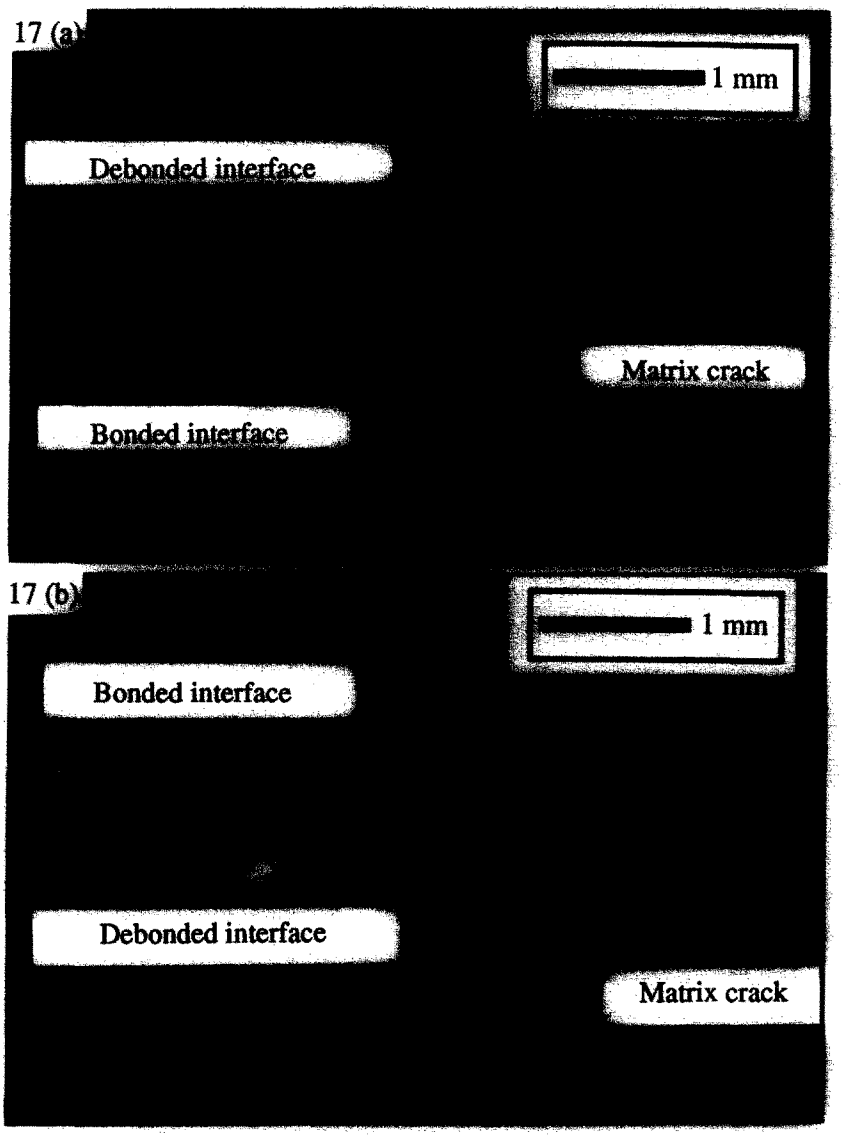

Fig. 17. Photographs of thin sections show that development of the debonding length for the first matrix crack with the increase of the applied stress as $f = 1.534\%$: (a) Debonding length observed at $\sigma_A = 4.8$ MPa [dash line (1) in Fig. 1]; (b) Debonding length observed at $\sigma_A = 6.4$ MPa [dash line (2) in Fig. 1.]; (c) Debonding length observed at $\sigma_A = 7.9$ MPa [dash line (3) in Fig. 1]; and (d) Debonding length observed at $\sigma_A = 11.$ MPa [dash line (4) in Fig. 1].

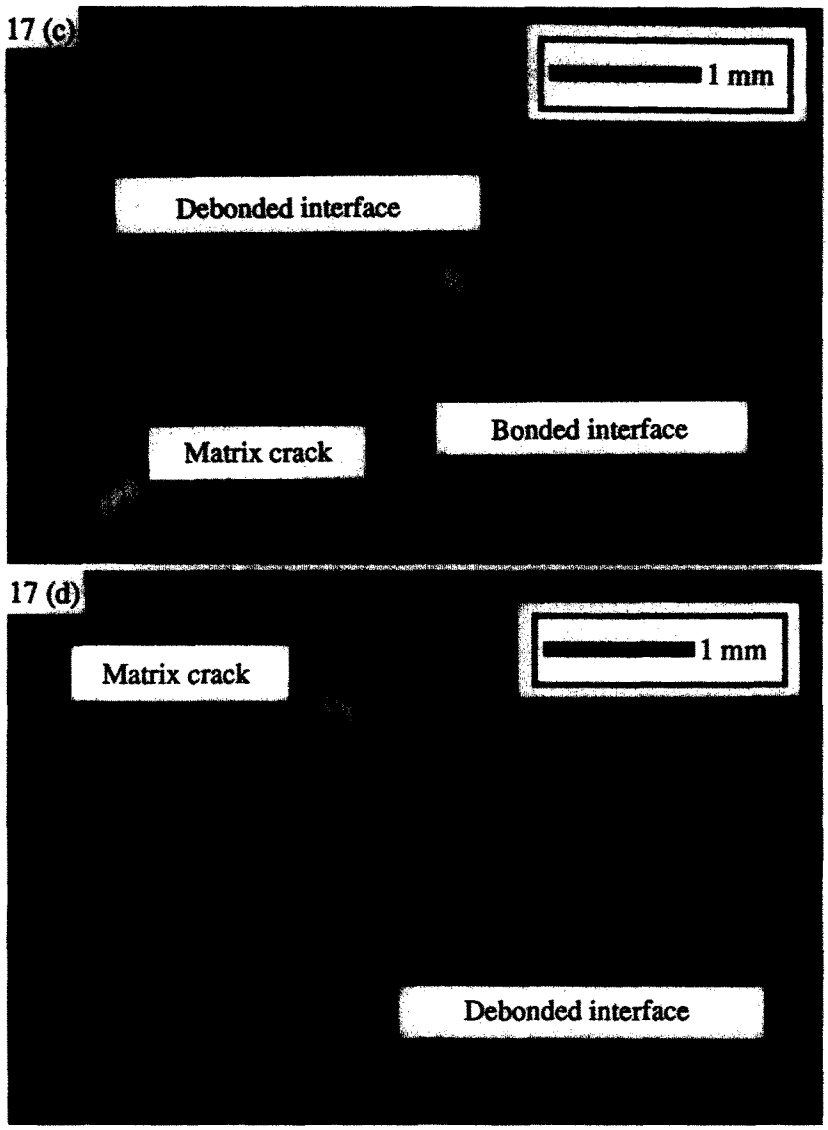

Fig. 17. (*continued*).

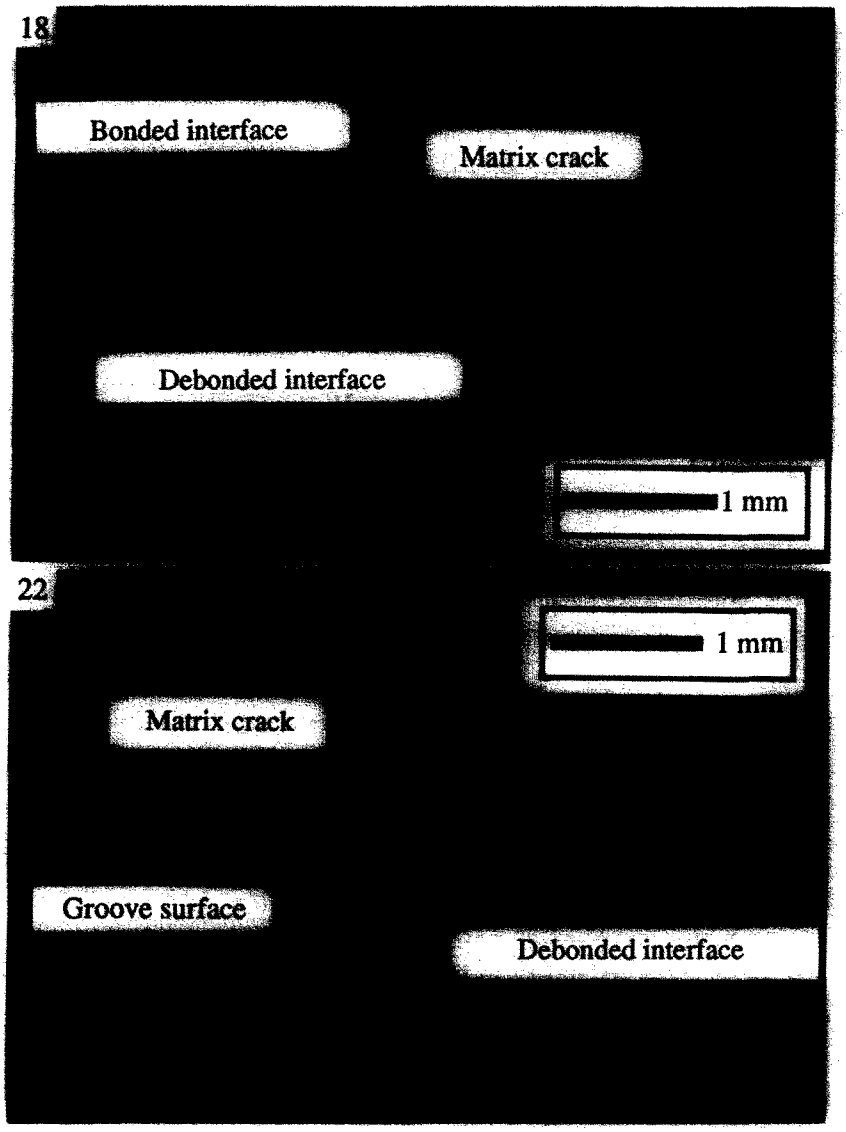

Fig. 18. An interface observed for the second matrix crack at $\sigma_A = 7.9$ MPa with $f = 1.534\%$. The debonding length is shorter than that observed in the first matrix crack [Fig. 18(c)] for the same stress level.

Fig. 22. The view of the groove interface for the first matrix crack of a specimen with $f = 6.135\%$ at $\sigma_A = 6.1$ MPa ($\sigma_A < \sigma_A^{BOP} = 6.92$ MPa). Very small debonding area is observed as compared to Fig. 18(b) for the close stress level.

debonding interface clearly, the fibers were taken out from the thin sections. A typical view of debonding zone after removing the fiber is shown in Fig. 16. The different brightness along the groove (fiber–matrix interface) of Fig. 16 is detectable to identify both the bonded and debonded regions. The transitional position (the ending zone of debonding) was decided using an OFM, which was used to place images from the thin sections into an image analysis system. Consequently, quantitative measurement of fracture process zone (debonding length) was achieved from that image.

6. EXPERIMENTAL RESULTS AND COMPARISON WITH ANALYTICAL PREDICTIONS

The methodology described above was applied to three series of specimens ($f = 0.767\%$, 1.534% and 6.135%), loaded up to specified values summarized in Table 2. A typical stress–strain curve of fiber volume fraction 1.534% is shown in Fig. 1. The four discrete loading levels (1), (2), (3) and (4) are indicated in this figure. For the steel fiber reinforced cement composite, a history of matrix cracks can be observed during the testing. Studies of OFM have revealed the growth of debonding at the fiber–matrix interface for a series of stress levels as shown in Fig. 17, where four debonding lengths at four discrete loading levels (shown in Fig. 1) are demonstrated. This observation is a typical one of fibers existing within a bridging zone. An increasing debonding length with respect to the applied stress observed from the micrographs proved the validity of the theoretical assumption of "stable growth" for the debonding crack.

It is also noted that the debonding lengths in the first few preceding cracks were longer than those in the succeeding cracks for the same stress level as can be seen by comparing Fig. 17(c) and Fig. 18. Such a phenomenon implies that the debonding length is a function of length l_c. However, the difference in debonding length among the latter preceding and succeeding cracks tends to become smaller. This can be explained as follows. As the load increases, the formation of new matrix cracks results in a decrease in the crack spacing, and then debonding growth is influenced by the crack spacing. The predicted dependence of the normalized debonding length for the first few matrix cracks with external stress (see Appendix D) is shown in Fig. 19 for $f = 0.767\%$ if $a/r \gg 1$ is considered. Analytical results agree well with the experimental measurement as shown in Fig. 20. The predicted results were obtained by using the material properties reported in Table 1(a) with $v_f = 0.3$ and $v_m = 0.2$, where surface energy of the matrix $\gamma = 7.5\ \mathrm{N\ m^{-1}}$, surface energy of the interface $\gamma^* = 5.5\ \mathrm{N\ m^{-1}}$ and frictional shear stress $\tau_f = 1.3$ MPa are from Li *et al.* (1991) and Jenq and Shah (1985). The analytical relationships between normalized debonding length and fiber volume fraction from eqn (15) for the first crack (plotted in Fig. 21) implies that the debonding behavior is more sensitive when the fiber volume fraction decreases (e.g. $f < 2\%$). The experimental observation of the present study shows that debonding phenomenon is retarded when fiber volume fraction increases [compare Figs 17(b) and 22].

Two sets of experimental data are evaluated for the external stress at the end point of multiple cracking. The results are listed in Table 3 with the analytical prediction determined by recursive computation between eqn (3) and eqn (D10) (see Appendix D). The first set of experimental results is from the present study. The second set is provided by Somayaji and Shah (1981). The predicted values were obtained by using the mechanical properties in

Table 2. The discrete loading levels for different volume fractions of steel fiber-reinforced cementitious composites

Fiber volume fraction (%)	Stage of stress level (MPa) (1)	(2)	(3)	(4)
0.767	2.2	3.1	3.3	3.8
1.534	4.8	6.4	7.9	11.0
6.135	4.2	6.1	11.0	18.0

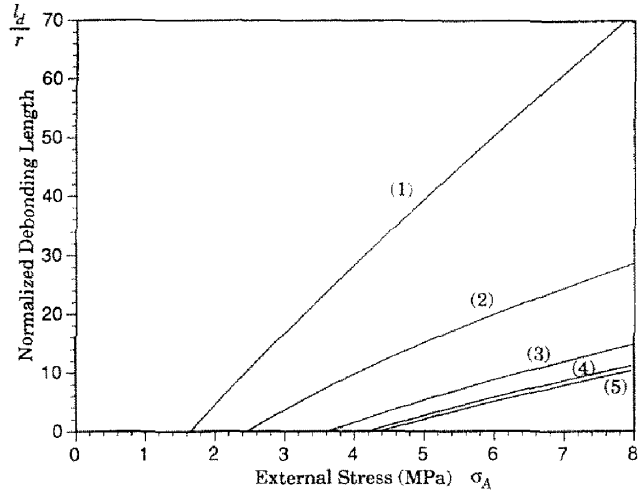

Fig. 19. Theoretical relationships between external stress and normalized debonding length with $f = 0.767\%$ and $r = 0.2$ mm for the first five matrix cracks are shown by using material properties reported in Table 1(a) with $\nu_f = 0.3$ and $\nu_m = 0.2$.

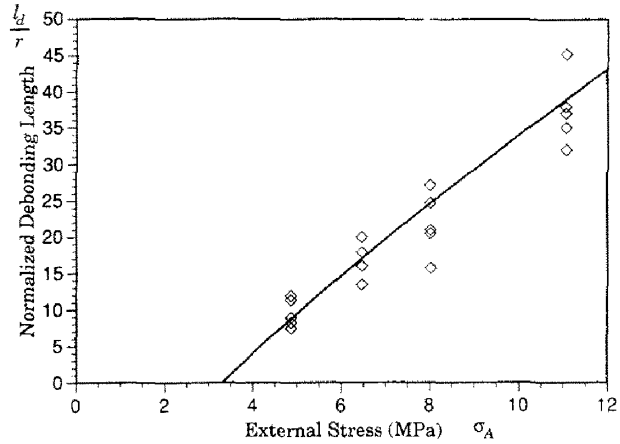

Fig. 20(a). Theoretical relationship between external stress and normalized debonding length ($f = 1.534\%$ and $r = 0.2$ mm) for the first matrix crack compares with experimental data points ◇ associated with crack No. 1 at discrete stress levels (shown in Table 2).

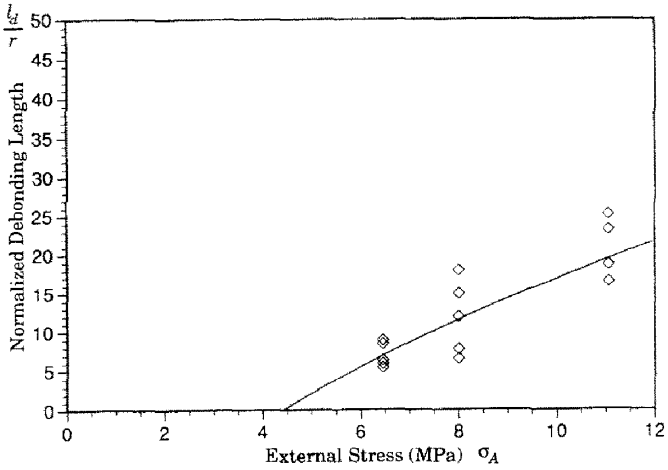

Fig. 20(b). Theoretical relationship between external stress and normalized debonding length ($f = 1.534\%$, $r = 0.2$ mm) for the second matrix crack compares with experimental data points ◇ associated with crack No. 2 at discrete stress levels (shown in Table 2).

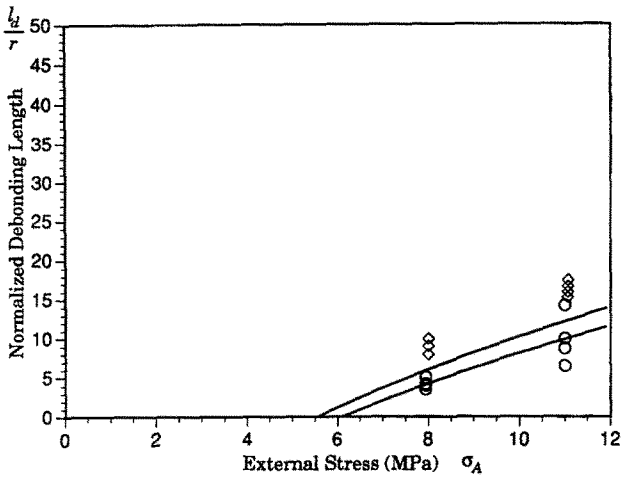

Fig. 20(c). Theoretical relationships between external stress and normalized debonding length ($f = 1.534\%$, $r = 0.2$ mm) for the third and fourth matrix cracks compare with experimental data points ◇ and ○ associated with cracks Nos 3 and 4 at discrete stress levels (shown in Table 2).

Table 3. Comparison of predicted stresses at the end point of multiple cracking with experimental results

Specimen set	Curing time (days)	Vf (%)	Fiber radius (mm)	Stress at EMC† Predicted (MPa)	Stress at EMC† Measured (MPa)
A (present study)	14	0.767	0.2	7.11	4.1
		1.534	0.2	8.91	8.77
		6.135	0.4	10.07	9.61
B (Somayaji *et al.*)	28	1.841	0.6	7.60	6.24
		2.761	0.6	9.29	8.06
		5.522	0.6	7.38	7.44
		2.454	0.8	8.70	7.65
		3.272	0.8	11.46	10.38

†EMC denotes the end point of multiple cracking.

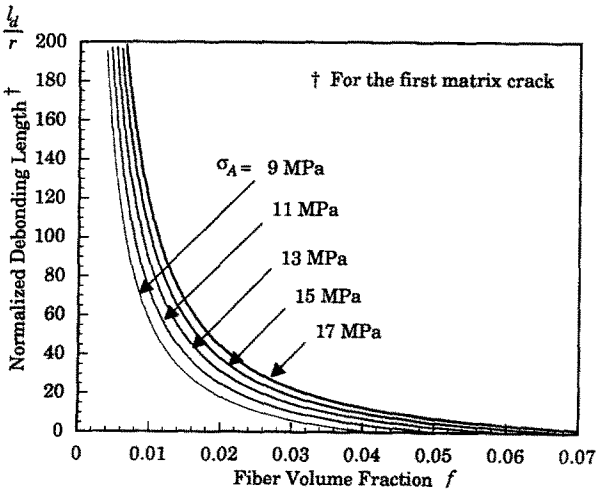

Fig. 21. The relationships between normalized debonding length and fiber volume fraction at different stress levels for the first matrix crack are shown by using mechanical properties in Table 1(a).

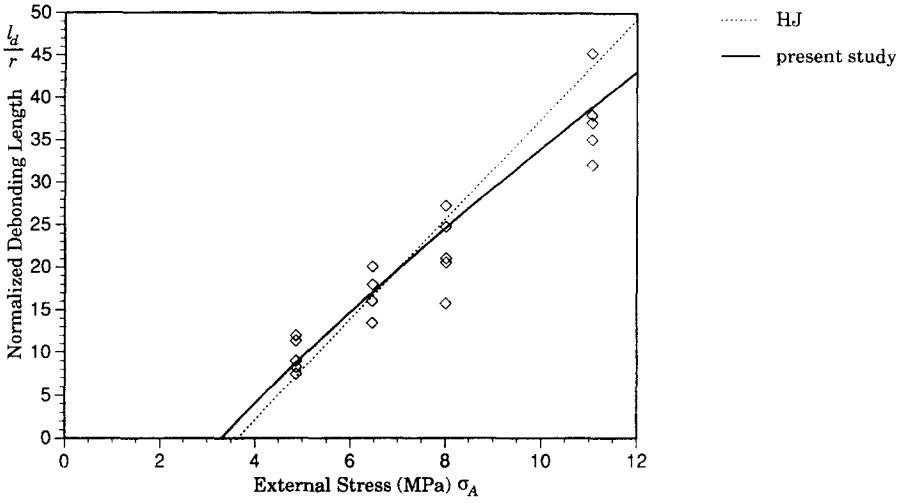

Fig. 23. Normalized debonding length as a function of external stress ($f = 1.534\%$, $r = 0.2$ mm) for the first matrix crack is shown by using material properties reported in Table 1(a). Comparison of present study and HJ's model with experimental data points ◇ at discrete stress levels.

Table 1(b). It can be seen that the theoretical predictions for the stress at the ending point of multiple fracture provide reasonable agreement with experimental data except for $f = 0.767\%$.

Another model to determine the debonding length for the case of constant friction proposed by Hutchinson and Jensen (1990) (HJ) has been used to compare with experimental results and the theoretical prediction described by eqn (15) for the case that the first matrix crack size is large, i.e. $a/r \gg 1$ and $r/l_c \to 0$. This comparison is shown in Fig. 23. According to the model in the present study and that of HJ, the debonding lengths denoted by l_d and l_d^{HJ} are determined respectively as follows:

$$\frac{l_d}{r} = \frac{\sigma_A}{2\tau_f}\frac{1}{f}\left\{1-\left[\frac{fE_f}{\bar{E}} + \frac{(1-f)E_m}{\bar{E}}\left(\frac{\sigma_A^i}{\sigma_A}\right)^2\right]^{1/2}\right\}, \tag{33}$$

$$\sigma_A^i = f\sigma_T^i = f\left(\frac{8E_f\gamma^*}{r}\right)^{1/2}, \tag{34}$$

and

$$\frac{l_d^{HJ}}{r} = \frac{\sigma_A}{2\tau_f}\frac{1-f}{c_3 f}\left(1-\frac{\sigma_A^{i(HJ)}}{\sigma_A}\right), \quad \sigma_A^{i(HJ)} = \frac{1}{c_1}\left(\frac{2E_m\gamma^*}{r}\right)^{1/2}, \tag{35, 36}$$

where σ_A^i is the applied stress of initial debonding for the present study and $\sigma_A^{i(HJ)}$ is for the HJ model. The nondimensional constants c_1 and c_3 are functions of E_m, E_f, ν_m and ν_f (Hutchinson and Jensen, 1990). Figure 23 indicates that the deviation of the threshold stress of initial debonding predicted by the present work and HJ's model is quite small. This suggests that the effect of Poisson's ratio is not significant for the stress at initial debonding in the steel-fiber, cement-based composite. Furthermore, for the higher loading the analytical predictions of present work are closer to the experimental results than those of HJ's constant frictional model. The HJ model overestimates the debonding length. This may be attributed in the absence of frictional consideration for the HJ's model, to when the jump condition in the fiber stress from above the tip to just below the tip is evaluated. Mathematically, it can also be demonstrated that the value of eqn (33) is smaller than that of eqn (35) when applied loading is large. Since eqn (33) has an extra term of order $(\sigma_A/\tau_f)^{1/2}$, which is a result of the frictional sliding effect. Therefore, it is evident that the

resistance of frictional sliding in the fracture criterion (energy balance analysis) plays an important role in determination of the extent of the debonding and cannot be ignored.

7. CONCLUSIONS

In the multiple cracking stage, fibers suppress the extension of matrix cracking through three effects: fiber bridging, interfacial debonding and frictional sliding. Debonding and sliding absorb part of the fracture energy. These effects are examined and formulated as enhanced toughness (increasing resistance) to the composites. The proposed relationships between the applied stress σ_A and the crack size a (Fig. 11) present the stability of a typical crack in the multiple cracking region and can explain the relationship between fracture process of multiple cracking and the stress–strain response of the composite. It is also shown that the interaction of two adjacent cracks is dependent on crack spacing. The amount of mechanical energy absorbed by interfacial debonding and frictional work in the multiple fracture increases the stress capacity. In turn, more cracks and the decrease in crack spacing are expected. With reference to the mechanics of debonding along fiber–matrix interfaces, it implies that the debonding can be suppressed by increased interfacial toughness, increased frictional shear stress and increased fiber volume fraction. The technique of OFM has been successfully used to observe and measure the interfacial failure in the steel fiber-reinforced cement composite. Finally, the predictions of the model compare favorably with measured values. It is shown that the extent of the debonding is a steady-state process rather than an unstable growth.

Acknowledgements—This research was supported by the National Science Foundation Center for Science and Technology of Advanced Cement-Based Materials (ACBM) Grant DMR-9120002 and partially supported by Air Force Office of Scientific research under grant F49620-92-J-0319.

REFERENCES

Aveston, J., Cooper, G. A. and Kelly, A. (1971). Single and multiple fracture. In *Conf. on The Properties of Fibre Composites*, National Physical Laboratory, Guildford, Surrey, pp. 15–26. IPC Science and Technology Press, Guildford, Surrey.

Aveston, J. and Kelly, A. (1973). Theory of multiple fracture of fibrous composites. *J. Mat. Sci.* **8,** 352–362.

Budiansky, B., Hutchinson, J. W. and Evans, A. (1986). Matrix fracture in fiber-reinforced ceramics. *J. Mech. Phys. Solids* **34**(2), 167–189.

Campbell, G. H., Rühle, M., Dalgleish, B. J. and Evans, A. G. (1990). Whisker toughening: a comparison between aluminum oxide and silicon nitride toughened with silicon carbide. *J. Am. Ceram. Soc.* **73**(3), 521–530.

Evans, A. G., Zok, F. W. and Davis, J. (1991). The role of interfaces in fiber-reinforced brittle matrix composites. *Compos. Sci. Technol.* **42,** 3–24.

Gao, Y. C., Mai, Y. W. and Cotterell, B. (1988). Fracture of fiber-reinforced materials. *J. Appl. Math. Phys. (ZAMP)* **39,** 550–572.

Gurney, C. and Hunt, J. (1967). Quasi-static crack propagation. *Philos. Trans. R. Soc. London, A* **299,** 508–524.

Hsueh, C. H. (1988). Elastic load transfer from partially embedded axially load fibre to matrix. *J. Mater. Sci. Lett.* **7,** 497–500.

Hutchinson, J. W. and Jensen, H. M. (1990). Models of fiber debonding and pullout in brittle composites with friction. *Mech. Mater.* **9,** 139–163.

Jenq, Y. and Shah, S. P. (1985). Two parameter fracture model for concrete. *J. Engng Mech. (ASME)* **111**(10), 1227–1241.

Li, S. H., Li, Z., Mura, T. and Shah, S. P. (1992). Multiple fracture of fiber reinforced brittle matrix composites based on micromechanics. *Engng Fract. Mech.* **43**(4), 561–579.

Li, Z., Mobasher, B. and Shah, S. P. (1991). Characterization of interfacial properties in fiber-reinforced cementitious composites. *J. Am. Ceram. Soc.* **74**(9), 2156–2164.

Marshall, D. B., Cox, B. N. and Evans, A. G. (1985). The mechanics of matrix cracking in brittle-matrix fiber composites. *Acta Metall.* **33**(11), 2013–2021.

Marshall, D. B. and Oliver, W. C. (1987). Measurement of interfacial mechanical properties in fiber-reinforced ceramic composites. *J. Am. Ceram. Soc.* **70**(8), 542–548.

Mindlin, R. D. (1953). Force at a point in the interior of a semi-infinite solid. *Proc. First Midwestern Conf. Solid Mech.*, pp. 56–59.

Mobasher, B., Stang, H. and Shah, S. P. (1990). Microcracking in fiber reinforced concrete. *Cem. Concr. Res.* **20**(5), 665–676.

Mori, T. and Tanaka, K. (1973). Average stress in matrix and average elastic energy of materials with misfitting inclusions. *Acta. Metall.* **21,** 571–574.

Mura, T. (1987). *Micromechanics of Defects in Solids* (2nd edn). Martinus Nijhoff, Dordrecht.

Nair, S. V. (1990). Crack-wake debonding and toughness in fiber- or whisker-reinforced brittle-matrix composites. *J. Am. Ceram. Soc.* **73**(10), 2839–2847.

Outwater, J. D. and Murphy, M. C. (1969). On the fracture energy of unidirectional laminate. In *Proceedings of*

24th Annual Technical Conf. of Reinforced Plastic Composites Division, Paper 11c. The Society of the Plastics Industry Inc., Composites Division, New York.
Penn, L. S. and Lee, S. M. (1989). Interpretation of experimental results in the single fiber pull-out test. *J. Comp. Tech. Res.* (*JCTRER*), **2**, 23–30.
Piggott, M. R. (1987). Debonding and friction at fiber polymer interfaces. 1. Criteria for failure and sliding. *Compos. Sci. Technol.* **30**, 295–306.
Shah, S. P. (1991). Do fibers increase tensile strength of concrete? *American Concrete Institute's Material Journal* **88**(6), 595–602.
Somayaji, S. and Shah, S. P. (1981). Bond stress versus slip relationship and cracking response of tension members. *ACI Jl* **78**(3), 217–225.
Sutcu, M. and Hillig, W. B. (1990). The effect of fiber-matrix debond energy on the matrix cracking strength and the debond shear strength. *Acta Metall. Mater.* **38**(12), 2653–2662.
Wells, J. K. and Beaumont, P. W. R. (1985). Debonding and pull-out processes in fibrous composites. *J. Mat. Sci.* **20**, 1275–1284.
Zhou, L. M., Kim, J. K. and Mai, Y. W. (1992). Interfacial debonding and fiber pull-out stresses. Part II: A new model based on the fracture mechanics approach. *J. Mat. Sci.* **27**, 3155–3166.
Zok, F., Sbaizero, O., Hom, C. L. and Evans, A. G. (1991). Mode-I fracture-resistance of a laminated fiber-reinforced ceramic. *J. Am. Ceram. Soc.* **74**(1), 187–193.

APPENDIX A. FIBER/MATRIX STRESSES IN THE ISOLATED-CYLINDRICAL ELEMENT AND DETERMINATION OF THE LENGTH l_c

Based on the shear lag model, the stresses of the fiber σ_f^A and matrix σ_m^A in the cylindrical element of a composite (Fig. 5) are given by

$$\sigma_f^A = \frac{E_f}{\bar{E}}\sigma_A + \left[\sigma_f^0 - \frac{E_f}{\bar{E}}\sigma_A\right]\exp -\sqrt{\eta}\frac{z'}{r}, \tag{A1}$$

and

$$\sigma_m^A = \frac{E_m}{E_f}\sigma_f^A - 2(\sigma_m^A|_{R=\lambda/2} - \frac{E_m}{E_f}\sigma_f^A)\frac{\ln(r'/r)}{\ln f}, \tag{A2}$$

with

$$\sigma_m^A|_{R=\lambda/2} = \frac{\sigma_A - [(1-E_m/E_f)f - (1-f)/\ln f(E_m/E_f)]\sigma_f^A}{1+(1-f)/\ln f}, \tag{A3}$$

$$\sigma_f^0 = \frac{\sigma_A}{f} - 2\tau_f\frac{l_d^{(0)}}{r}, \tag{A4}$$

$$\sigma_m^0 = 2\tau_f\frac{f}{(1-f)}\frac{l_d^{(0)}}{r}, \tag{A5}$$

and

$$\eta = -\frac{2\bar{E}/E_f}{(1+\nu_m)[(1-f)+\ln f]}, \tag{A6}$$

where z' is the distance parallel with the fiber's axis from the plane of debonding crack tip $x_3 = 0$ (Fig. 5) and σ_A is the far field stress. $l_d^{(0)}$ is the previous debonding length in the first crack. ν_m is Poisson's ratio of the matrix, f is the volume fraction of the fiber. E_f and E_m are Young's moduli for the fiber and matrix. $\bar{E}$, defined by $\bar{E} = fE_f + (1-f)E_m$, is Young's modulus of the composite. The stress in the fiber σ_f^A is related to the interfacial shear stress τ_r based on the equilibrium condition $d\sigma_f^A/dz' = -2\tau_r/r$ at all positions along the fiber's axis. Thus, a combination of the equilibrium condition $d\sigma_f^A/dz' = -2\tau_r/r$ and eqn (A1) gives the interfacial shear stress τ_r in the form of

$$\tau_r = \frac{\sqrt{\eta}}{2}\left(\sigma_f^0 - \frac{E_f\sigma_A}{\bar{E}}\right)\exp -\sqrt{\eta}\frac{z'}{r}. \tag{A7}$$

As mentioned earlier, the succeeding matrix crack does not initiate until the matrix stress reaches the critical value σ_{mu}. This ultimate strength depends on material properties and fiber volume fraction (Aveston *et al.*, 1971). Combining eqn (A2) and this criterion, the length l_c can be determined as

$$\frac{l_c}{r} = \frac{-1}{\sqrt{\eta}}\ln\left[-\frac{(A\sigma_A/f + B\sigma_f^\infty - \sigma_{mu})}{B(\sigma_f^0 - \sigma_f^\infty)}\right], \tag{A8}$$

where

$$\sigma_f^\infty = \frac{E_f}{\bar{E}}\sigma_A, \tag{A9}$$

$$A = \frac{f}{[1+(1-f)/\ln f)]}, \tag{A10}$$

and

$$B = \frac{-[(1-E_m/E_f)f-(E_m/E_f)(1-f)/\ln f]}{[1+(1-f)/\ln f)]}. \tag{A11}$$

If σ_A goes to infinity, the asymptotic value of the length l_c from eqn (A8) will approach a constant value, i.e.

$$\frac{[l_c]_{asym.}}{r} = \frac{-1}{\sqrt{\eta}} \ln\left[-\frac{D\bar{E}}{B(1-f)E_m}\right], \tag{A12}$$

where

$$D = A + B\frac{fE_f}{\bar{E}}. \tag{A13}$$

APPENDIX B. DERIVATIONS OF BRIDGING STRESS AND BRIDGING FACTOR

The stress disturbance due to the presence of inhomogeneity (e.g. a matrix crack) in a body subjected to external stresses can be simulated by an eigenstress caused by a fictitious misfit strain (eigenstrain) in the body. This kind of equivalency is called the equivalent inclusion method (Mura, 1987). In this study, the eigenstrain ε_p is introduced to simulate a matrix crack without the region of fiber bridging and another eigenstrain $\alpha\varepsilon_p$ is to simulate the region of a crack bridged by fibers. In order to find the stress in Ω_0 caused by a uniform eigenstrain $\varepsilon^*_{33} = \varepsilon_p$ for a semi-infinite body shown in part (i) of Fig. 6, we define Green's functions $G_{ij}(\mathbf{x}, \mathbf{x}')$ satisfying the following equations (Mura, 1987): for $x_3 \geqslant 0$,

$$C_{ijkl}G_{km,lj}(\mathbf{x}, \mathbf{x}') + \delta_{im}\delta(\mathbf{x}, \mathbf{x}') = 0; \tag{B1}$$

on $x_3 = 0$,

$$C_{ijkl}G_{km,l}(\mathbf{x}, \mathbf{x}')n_j = \delta_{im}\delta_s(\mathbf{x}, \mathbf{x}'), \tag{B2}$$

where C_{ijkl} are the elastic moduli. The Einstein summation convention for the repeated indices is employed. $\delta(\mathbf{x}, \mathbf{x}')$ and $\delta_s(\mathbf{x}, \mathbf{x}')$ are the three and two-dimensional Dirac delta functions, respectively. They have properties as follows:

$$\int_0^\infty f(\mathbf{x}')\delta(\mathbf{x}, \mathbf{x}')\,d\mathbf{x}' = f(\mathbf{x}), \tag{B3}$$

and

$$\int_s f(\mathbf{x}')\delta_s(\mathbf{x}, \mathbf{x}')\,ds(\mathbf{x}') = f(\mathbf{x}). \tag{B4}$$

Green's functions $G_{ij}(\mathbf{x}, \mathbf{x}')$ for the half space isotropic medium have been derived by Mindlin (1953). Therefore, the displacement $u_i(\mathbf{x})$ due to $\varepsilon^*_{33} = \varepsilon_p$ in domain Ω_0 is written as

$$\begin{aligned} u_i(\mathbf{x}) &= C_{jlmn}\varepsilon^*_{mn}\int_{\Omega_0}\frac{\partial}{\partial x'_l}G_{ij}(\mathbf{x}, \mathbf{x}')\,d\mathbf{x}' \\ &= \bar{\lambda}\varepsilon_p\int_{\Omega_0}\frac{\partial}{\partial x'_j}G_{ij}\,d\mathbf{x}' + 2\bar{\mu}\varepsilon_p\int_{\Omega_0}\frac{\partial}{\partial x'_3}G_{i3}\,d\mathbf{x}', \end{aligned} \tag{B5}$$

where $\bar{\lambda} = 2\bar{\mu}\bar{\nu}/(1-2\bar{\nu})$; $\bar{\mu}$ and $\bar{\nu}$ are the average shear modulus and Poisson's ratio of the composite, both determined by the law of mixtures. The $\sigma_{33}(\mathbf{x})$ component of internal stress in domain Ω_0 is in the form of

$$\begin{aligned} \sigma_{33}(\mathbf{x}) &= (\bar{\lambda}+2\bar{\mu})(\varepsilon_{33}-\varepsilon_p)+\bar{\lambda}(\varepsilon_{11}+\varepsilon_{22}) \\ &= \frac{2\bar{\mu}}{1-2\bar{\nu}}\bar{\nu}(u_{1,1}+u_{2,2})+\frac{2\bar{\mu}}{1-2\bar{\nu}}(1-\bar{\nu})(u_{3,3}-\varepsilon_p) \\ &= \left\{\frac{\bar{\mu}\bar{\nu}\varepsilon_p}{4\pi(1-2\bar{\nu})(1-\bar{\nu})}\left[-2\bar{\nu}\Phi_{,11}(\mathbf{x})-2\bar{\nu}\Phi_{,22}(\mathbf{x})-2(1-\bar{\nu})\Phi_{,33}(\mathbf{x})+\frac{\partial}{\partial x_1}\int_{\Omega_0}(x_1-x'_1)\left[\frac{-1}{R_1^3}-\frac{3(x_3-x'_3)^2}{R_1^5}\right]d\mathbf{x}'\right.\right. \\ &\quad +\frac{\partial}{\partial x_2}\int_{\Omega_0}(x_2-x'_2)\left[\frac{-1}{R_1^3}-\frac{3(x_3-x'_3)^2}{R_1^5}\right]d\mathbf{x}'+\frac{(1-\bar{\nu})}{\bar{\nu}}\frac{\partial}{\partial x_3}\int_{\Omega_0}\left[(-1+4\bar{\nu})\left(\frac{1}{R_1}\right)_{,3}\right. \\ &\quad \left.\left.+\frac{3(x_3-x'_3)^3}{R_1^5}\right]d\mathbf{x}'-\frac{8\pi(1-\bar{\nu})^2}{\bar{\nu}}\right]\Bigg\}+\left\{\frac{\bar{\mu}\bar{\nu}\varepsilon_p}{4\pi(1-2\bar{\nu})(1-\bar{\nu})}\left[-2\bar{\nu}(3-4\bar{\nu})[\Psi_{,11}(\mathbf{x})+\Psi_{,22}(\mathbf{x})]\right.\right. \\ &\quad -4\bar{\nu}x_3[\Psi_{,311}(\mathbf{x})+\Psi_{,322}(\mathbf{x})]+2(1-\bar{\nu})(3-4\bar{\nu})\Psi_{,33}(\mathbf{x})-4(1-\bar{\nu})\Psi_{,33}(\mathbf{x})-4(1-\bar{\nu})x_3\Psi_{,333}(\mathbf{x}) \\ &\quad \left.\left.+\frac{\partial}{\partial x_1}\int_{\Omega_0}(x_1-x'_1)\phi\,d\mathbf{x}'+\frac{\partial}{\partial x_2}\int_{\Omega_0}(x_2-x'_2)\phi\,d\mathbf{x}'+\frac{(1-\bar{\nu})}{\bar{\nu}}\frac{\partial}{\partial x_3}\int_{\Omega_0}\varphi\,d\mathbf{x}'\right]\right\}, \end{aligned} \tag{B6}$$

where

$$R_1^2 = (x_1 - x_1')^2 + (x_2 - x_2')^2 + (x_3 - x_3')^2, \tag{B7}$$

$$R_2^2 = (x_1 - x_1')^2 + (x_2 - x_2')^2 + (x_3 + x_3')^2, \tag{B8}$$

$$\Phi(\mathbf{x}) = \int_{\Omega_0} \frac{1}{R_1} \mathrm{d}\mathbf{x}', \quad \Psi(\mathbf{x}) = \int_{\Omega_0} \frac{1}{R_2} \mathrm{d}\mathbf{x}', \tag{B9, 10}$$

$$\phi(\mathbf{x}, \mathbf{x}') = \frac{-(3-4\bar{\nu})}{R_2^3} + \frac{6x_3(x_3+x_3')}{R_2^5} + \frac{6x_3x_3'}{R_2^5} - \frac{3(3-4\bar{\nu})(x_3^2 - x_3'^2)}{R_2^5} - \frac{30x_3x_3'(x_3+x_3')^2}{R_2^7} + \frac{4(1-\bar{\nu})(1-2\bar{\nu})}{R_2(R_2+x_3+x_3')^2} + \frac{4(1-\bar{\nu})(1-2\bar{\nu})(2R_2+x_3+x_3')(x_3+x_3')}{R_2^3(R_2+x_3+x_3')^2}, \tag{B11}$$

$$\varphi(\mathbf{x}, \mathbf{x}') = [8(1-\bar{\nu})^2 - 3(3-4\bar{\nu})]\left(\frac{1}{R_2}\right)_{,3} + 2x_3\left(\frac{1}{R_2}\right)_{,33} + 2x_3x_3'\left(\frac{1}{R_2}\right)_{,333} - \frac{3(3-4\bar{\nu})(x_3+x_3')^3}{R_2^5}. \tag{B12}$$

In the right-hand side of eqn (B6), there are two terms quoted within two pairs of curvy braces. Physically, the first term in the right of eqn (B6) leads to the solution of infinite body case, and the second term can be treated as the residual term caused by opposite traction of the first term on the surface $x_3 = 0$. The eigenstrain ε_p in Ω_0 causes a non-uniform stress $\sigma_{33}(\mathbf{x})$. In order to provide simplicity, the average internal stress $\langle\sigma_{33}\rangle^{(i)}$ in Ω_0 is taken as

$$\langle\sigma_{33}\rangle_{\Omega_0}^{(i)} = -\frac{\bar{\mu}\pi c\varepsilon_p}{2(1-\bar{\nu})a}\left[1 + \beta(\bar{\nu})\left(\frac{a}{l_c}\right)^n\right], \tag{B13}$$

where "$\langle\ \rangle$" denotes the average and the domain is defined in subscript. $\beta(\bar{\nu})$ is a factor determined from the second term of eqn (B6) through numeric calculation, and the value of power n must be not less than 1. If we consider the average forms in Mori and Tanaka's theory (Mori and Tanaka, 1973), the average stresses $\langle\sigma_{33}\rangle^{(ii)}$ in Ω and $\Omega_0 - \Omega$ subjected to a uniform eigenstrain $\varepsilon_{33}^* = -(1-\alpha)\varepsilon_p$ in Ω [part (*ii*) of Fig. 6] are shown as follows:

$$\langle\sigma_{33}\rangle_{\Omega}^{(ii)} = (1-f)\frac{\bar{\mu}\pi c(1-\alpha)\varepsilon_p}{2(1-\bar{\nu})r}, \tag{B14}$$

$$\langle\sigma_{33}\rangle_{\Omega_0-\Omega}^{(ii)} = -\frac{f\bar{\mu}\pi c(1-\alpha)\varepsilon_p}{2(1-\bar{\nu})r}. \tag{B15}$$

Consequently, the stress disturbances $\langle\sigma_f^{\text{Dist.}}\rangle$ in bridged part Ω and $\langle\sigma_m^{\text{Dist.}}\rangle$ in unbridged part $\Omega_0 - \Omega$ caused by the eigenstrain ε_{33}^* are the sum of eqn (B13) and eqns (B14)–(B15). They are given by

$$\langle\sigma_m^{\text{Dist.}}\rangle = \langle\sigma_{33}\rangle_{\Omega_0-\Omega} = -\frac{\bar{\mu}\pi c\varepsilon_p}{2(1-\bar{\nu})a}\left[1 + \beta(\bar{\nu})\left(\frac{a}{l_c}\right)^n\right] - \frac{f\bar{\mu}\pi c(1-\alpha)\varepsilon_p}{2(1-\bar{\nu})r}, \tag{B16}$$

and

$$\langle\sigma_f^{\text{Dist.}}\rangle = \langle\sigma_{33}\rangle_{\Omega} = -\frac{\bar{\mu}\pi c\varepsilon_p}{2(1-\bar{\nu})a}\left[1 + \beta(\bar{\nu})\left(\frac{a}{l_c}\right)^n\right] + (1-f)\frac{\bar{\mu}\pi c(1-\alpha)\varepsilon_p}{2(1-\bar{\nu})r}. \tag{B17}$$

The value of ε_p for fibers inside the matrix crack calculated by the traction-free condition in the crack surface is given by

$$\varepsilon_p = \frac{2(1-\bar{\nu})a}{\bar{\mu}\pi c[1 + \beta(a/l_c)^n + (1-\alpha)f(a/r)]}\xi\sigma_A, \tag{B18}$$

where

$$\xi = \left[1 + \frac{(1-f)}{f}\frac{E_m}{E_f}\exp -\sqrt{\eta}\frac{l_c}{r}\right]. \tag{B19}$$

Based on the assumption of this model that the size of the matrix crack bridged by fibers should be larger than the fiber radius and for moderately small fiber volume fraction, the bridging stress σ_T can be obtained and simplified from the linear superposition of the uncracked part and disturbance part, which is

$$\sigma_T = \frac{(1-\alpha)a/r}{1 + \beta(a/l_c)^n + (1-\alpha)f(a/r)}\xi\sigma_A. \tag{B20}$$

Provided that the bridging stress σ_T placed upon the fibers must be greater than zero as a/r goes to ∞, the value

of n can only be 1. In addition, it can be pointed out from eqn (B20) that σ_T depends on crack size, length l_c and applied stress. But the factor α is still undetermined in this equation. If the slip region is considered near the crack surface, the axial stresses in a fiber $\sigma_f(z)$ and matrix $\sigma_m(z)$ can be obtained by the force equilibrium with the assumption of constant frictional shear stress τ_f. They are given by

$$\sigma_f(z) = \sigma_T - 2\tau_f\left(\frac{z}{r}\right), \tag{B21}$$

$$\sigma_m(z) = 2\tau_f \frac{f}{1-f}\left(\frac{z}{r}\right), \tag{B22}$$

where z is the distance measured from the crack surface parallel with the fiber's direction. The tensile strains in the fiber and matrix are σ_f/E_f and σ_m/E_m. Therefore, displacements of the fiber $U_f(z)$ and matrix $U_m(z)$ are obtained by integrating the strains with respect to z. These are as follows:

$$U_f(z) = \int_z^l \frac{\sigma_f}{E_f}\,dz = \frac{\sigma_T}{E_f}(l-z) - \frac{\tau_f}{E_f}\left(\frac{l^2-z^2}{r}\right), \tag{B23}$$

$$U_m(z) = \int_z^l \frac{\sigma_m}{E_m}\,dz = \frac{\tau_f}{E_m}\frac{f}{1-f}\left(\frac{l^2-z^2}{r}\right). \tag{B24}$$

The slip distance l of the fiber is determined by using the condition $\varepsilon_m = \varepsilon_f$ at $z = l$, which is

$$l = \frac{(1-f)}{2}\frac{\sigma_T}{\tau_f}\frac{E_m}{\bar{E}}r. \tag{B25}$$

Consequently, the crack opening U_{cod} for both sides of the matrix crack can be obtained by calculating the displacement difference between the fiber $U_f(z)$ and matrix $U_m(z)$ at the crack surface plane, i.e.

$$\begin{aligned} U_{cod} &= 2(U_f - U_m)|_{z=0} \\ &= \frac{(1-f)rE_m/E_f}{2\tau_f\bar{E}}\left\{\frac{(1-\alpha)a/r}{[1+\beta(a/l_c)+(1-\alpha)(a/r)f]}\right\}^2\xi^2\sigma_A^2. \end{aligned} \tag{B26}$$

Referring to the equivalent inclusion method, the crack opening displacement U_{cod} is equal to $2c\alpha\varepsilon_p$. It implies $2c\alpha\varepsilon_p = 2(U_f - U_m)|_{z=0}$. After some algebraic manipulation, the bridging factor α can be determined as

$$\alpha = \frac{1}{2(a/r)(f+\kappa)}\left\{1+\frac{a}{r}\left[2\kappa+f+\beta\left(\frac{r}{l_c}\right)\right] - \left\{\left\{1+\frac{a}{r}\left[2\kappa+f+\beta\left(\frac{r}{l_c}\right)\right]\right\}^2 - 4\kappa(f+\kappa)\left(\frac{a}{r}\right)^2\right\}^{1/2}\right\}, \tag{B27}$$

where

$$\kappa = \frac{\pi\bar{\mu}(1-f)E_m}{8\tau_f(1-\bar{\nu})E_f\bar{E}}\xi\sigma_A. \tag{B28}$$

APPENDIX C. ENERGY CHANGES WITH THE EXTENSION OF A DEBONDING CRACK

A cylindrical model is proposed to simulate a fiber–matrix element in a crack. The size of matrix crack remains unchanged when the fiber starts to debond up to l_d. Therefore:

(i) The strain energy in the fiber and matrix

$$\begin{aligned} W_E &= \frac{\pi r^2}{2E_f}\int_0^{l_d}\sigma_f^2\,dz + \frac{f}{(1-f)}\frac{\pi r^2}{2E_m}\int_0^{l_d}\sigma_m^2\,dz \\ &= \frac{\pi r^2\tau_f^2}{2E_f}\left\{\frac{4}{3}\frac{\bar{E}}{(1-f)E_m}\frac{l_d^3}{r^2} - 2\frac{\sigma_T}{\tau_f}\frac{l_d^2}{r} + \left(\frac{\sigma_T}{\tau_f}\right)^2 l_d\right\}, \end{aligned} \tag{C1}$$

and

$$\begin{aligned} dW_E &= \frac{\partial W_E}{\partial(2\pi r l_d)}\cdot 2\pi r d(l_d) \\ &= \frac{r\tau_f^2}{4E_f}\left[\frac{\sigma_T^2}{\tau_f^2} + \frac{4}{(1-f)}\frac{\bar{E}}{E_m}\left(\frac{l_d}{r}\right)^2 - 4\frac{\sigma_T}{\tau_f}\left(\frac{l_d}{r}\right)\right]\cdot 2\pi r d(l_d). \end{aligned} \tag{C2}$$

Here, the contribution of matrix shear deformation is ignored. However, if the matrix is much more compliant than the fiber, the matrix shear deformation may be taken into account in dW_E (Piggott, 1987; Penn and Lee, 1989; Zhou *et al.*, 1992);

(ii) The work done against the frictional sliding

$$W_F = 2\pi r\tau_f \int_0^{l_d} (U_f - U_m)\,dz$$
$$= -\tfrac{4}{3}\pi r^2\tau_f^2 f\left[\frac{1}{(1-f)E_m} + \frac{1}{fE_f}\right]\frac{l_d^3}{r^2} + \pi r^2\tau_f \frac{\sigma_T}{E_f}\frac{l_d^2}{r}, \tag{C3}$$

and

$$dW_F = \frac{\partial W_F}{\partial(2\pi r l_d)}\cdot 2\pi r d(l_d)$$
$$= \frac{r\tau_f^2}{E_f}\left[-\frac{2}{(1-f)}\frac{\bar{E}}{E_m}\left(\frac{l_d}{r}\right)^2 + \frac{\sigma_T}{\tau_f}\left(\frac{l_d}{r}\right)\right]\cdot 2\pi r d(l_d); \tag{C4}$$

(iii) The work done by the bridging force

$$W_L = -\pi r^2\sigma_T(U_f - U_m)|_{z=0}$$
$$= \frac{\pi r^2\tau_f^2}{E_f}\left\{-\left(\frac{\sigma_T}{\tau_f}\right)^2 l_d + \frac{\bar{E}}{(1-f)E_m}\frac{\sigma_T}{\tau_f}\frac{l_d^2}{r}\right\}, \tag{C5}$$

and

$$dW_L = \frac{\partial W_L}{\partial(2\pi r l_d)}\cdot 2\pi r d(l_d)$$
$$= \frac{r\tau_f^2}{2E_f}\left[-\frac{\sigma_T^2}{\tau_f^2} + \frac{2}{(1-f)}\frac{\bar{E}}{E_m}\frac{\sigma_T}{\tau_f}\left(\frac{l_d}{r}\right)\right]\cdot 2\pi r d(l_d); \tag{C6}$$

(iv) The surface energy created by debonding is

$$W_{\gamma^*} = 4\pi r\gamma^* l_d, \tag{C7}$$

and

$$dW_{\gamma^*} = \frac{\partial W_{\gamma^*}}{\partial(2\pi r l_d)}\cdot 2\pi r d(l_d)$$
$$= 2\gamma^*\cdot 2\pi r d(l_d). \tag{C8}$$

APPENDIX D. THE PROCESS OF INTERFACIAL DEBONDING GROWTH

If we consider $a/r \gg 1$, the values of α, σ_T, G, ΔG_S and ΔG_D can be simplified as follows:

(i) The factor α, i.e. eqn (6), becomes

$$\alpha \cong \frac{\left[2\kappa + f + \beta\left(\frac{r}{l_c}\right)\right] - \left\{\left[f + \beta\left(\frac{r}{l_c}\right)\right]^2 + 4\kappa\beta\left(\frac{r}{l_c}\right)\right\}^{1/2}}{2(f+\kappa)}, \tag{D1}$$

and

$$\frac{\partial\alpha}{\partial a} \cong 0; \tag{D2}$$

(ii) The bridging stress σ_T from eqn (5) becomes

$$\sigma_T(a/r \gg 1) = \frac{(1-\alpha)\xi\sigma_A}{\beta(r/l_c) + (1-\alpha)f}; \tag{D3}$$

(iii) The expressions of ΔG_S, ΔG_D and G can also be simplified by substituting eqn (D2) into eqns (26), (27) and (31)

$$\Delta G_S \cong C_s(1-\alpha)^3\frac{[5\Gamma^3 + 2\Lambda\Gamma^4 + 2(1-\alpha)\Gamma^4 f]}{[1+\Gamma\Lambda+(1-\alpha)\Gamma f]^4}\xi^3\sigma_A^3, \tag{D4}$$

$$\Delta G_D \cong C_d(1-\alpha)\frac{[3\Gamma + 2(1-\alpha)\Gamma^2 f + 2\Lambda\Gamma^2]}{[1+\Gamma\Lambda+(1-\alpha)\Gamma f]^2}\xi\sigma_A, \tag{D5}$$

$$G \cong C_f\left\{\frac{3\Gamma + 5\Lambda\Gamma^2 + 2\Lambda^2\Gamma^3}{[1+\Gamma\Lambda+(1-\alpha)\Gamma f]^3} + (1-\alpha)\frac{(4\alpha+5)\Gamma^2 f + 2\Lambda\Gamma^3 f}{[1+\Gamma\Lambda+(1-\alpha)\Gamma f]^3} + (1-\alpha^2)\frac{2(1-\alpha)\Gamma^3 f^2 + 2\Lambda\Gamma^3 f}{[1+\Gamma\Lambda+(1-\alpha)\Gamma f]^3}\right\}\xi^2\sigma_A^2, \tag{D6}$$

where

$$C_s = \frac{f(1-f)^2 E_m^2 r}{12\tau_f E_f \bar{E}^2}, \tag{D7}$$

$$C_d = \frac{f(1-f)E_m\gamma^*}{\tau_f \bar{E}}, \tag{D8}$$

$$C_f = \frac{2(1-\bar{\nu})}{3\pi\bar{\mu}} r. \tag{D9}$$

The first complete matrix cracking stress σ_{A1} (see Fig. 11 for definition) can be solved from the following equation by inserting (D4), (D5) and (D6) into eqn (32), and letting $\Lambda = 0$ $(r/l_c \to 0)$

$$C_s\xi^3\sigma_A^3 - C_f\xi^2\frac{[\Lambda f+\Lambda^2(1-\alpha^2)f^2+(1+\alpha)]}{(1-\alpha)^2}\sigma_A^2 + C_d\xi\frac{[\Lambda+(1-\alpha)f]^2}{(1-\alpha)^2}\sigma_A + \frac{[\Lambda+(1-\alpha)f]^3}{(1-\alpha)^3}\gamma = 0. \tag{D10}$$

The debonding length l_d in the first crack is a function of applied stress σ_A by substituting σ_T [eqn (D3) with $\Lambda = 0(r/l_c \to 0)$] into eqn (15), that is

$$\frac{l_d}{r} = \frac{\sigma_A}{2\tau_f}\frac{1}{f}\left\{1-\left[\frac{fE_f}{\bar{E}} + \frac{(1-f)E_m}{\bar{E}}\left(\frac{\sigma_A^i}{\sigma_A}\right)^2\right]^{1/2}\right\}, \tag{D11}$$

where

$$\sigma_A^i = f\left(\frac{8E_f\gamma^*}{r}\right)^{1/2}. \tag{D12}$$

When applied stress reaches σ_{A1}, the debonding length $l_d^{(0)}$ and the length l_c between the first and second cracks can then be determined from eqns (D11) and (3). Similarly, the second matrix cracking stress σ_{A2} is obtained by solving eqn (D10) and letting $\Lambda = \beta(r/l_c)$. Also, the debonding length in the second crack as a function of applied stress can be calculated from eqn (15), where σ_T is given by (D3) with $\Lambda = \beta(r/l_c)$. The matrix cracking stress and debonding length of the succeeding cracks (e.g. crack Nos. 3, 4, etc.) can be determined by using this procedure. During the stage of multiple cracking, the increment of the applied stress decreases as the number of cracks increases. Consequently, when the applied stress reaches the ending point of multiple cracking, the matrix cracking propagates into a set of blocks and the crack spacing turns into a constant value. Each of the curves shown in Fig. 19 represents the debonding length at a given crack (1, 2, 3, ..., etc.).